Surface Science Reports 66 (2011) 1–27

Contents lists available at ScienceDirect

Surface Science Reports

journal homepage: www.elsevier.com/locate/surfrep

Kelvin probe force microscopy and its application

Wilhelm Melitz [a,b], Jian Shen [a,b], Andrew C. Kummel [a], Sangyeob Lee [a,*]

[a] Department of Chemistry and Biochemistry, University of California, San Diego, La, Jolla, CA 92093, USA

[b] Materials Science & Engineering Program, University of California, San Diego, La, Jolla, CA 92093, USA

ARTICLE INFO

Article history:
Accepted 18 October 2010
editor: W.H. Weinberg

Keywords:
Kelvin probe force microscopy
Scanning probe miscroscopy

ABSTRACT

Kelvin probe force microscopy (KPFM) is a tool that enables nanometer-scale imaging of the surface potential on a broad range of materials. KPFM measurements require an understanding of both the details of the instruments and the physics of the measurements to obtain optimal results. The first part of this review will introduce the principles of KPFM and compare KPFM to other surface work function and potential measurement tools, including the Kelvin probe (KP), photoemission spectroscopy (PES), and scanning electron microscopy (SEM) with an electron beam induced current (EBIC) measurement system. The concept of local contact potential difference (LCPD), important for understanding atomic resolution KPFM, is discussed. The second part of this review explores three applications of KPFM: metallic nanostructures, semiconductor materials, and electrical devices.

© 2010 Elsevier B.V. All rights reserved.

Contents

1. Introduction 1
2. Principles of scanning Kelvin probe force microscopy 2
  2.1. Basic principle of atomic force microscopy 2
  2.2. Kelvin probe force microcopy 3
    2.2.1. Fundamentals of KPFM 3
    2.2.2. KPFM operational mode: FM and AM mode 4
    2.2.3. KPFM instrumentation and preparation of conducting AFM tip 5
    2.2.4. Comparison of KPFM to other surface potential measurement systems 6
    2.2.5. High-resolution KPFM: concept of LCPD 6
3. Application of high-resolution KPFM 11
  3.1. Electrical properties of metallic nanostructures 11
    3.1.1. KPFM on metallic nanostructures 11
    3.1.2. Charge transfer in metallic nanostructure catalyst 12
  3.2. Characterization of electrical properties on semiconductor nanostructures 14
    3.2.1. KPFM on semiconductor surfaces 14
    3.2.2. Adsorbates on semiconductor surfaces 16
  3.3. Nano-scale electrical properties characterization in devices 17
    3.3.1. Quantum dots 17
    3.3.2. Junctions and heterostructures 18
    3.3.3. Transistors 20
    3.3.4. Solar cells 23
4. Concluding remarks 26
  Acknowledgements 26
  References 26

1. Introduction

Kelvin probe force microscopy, or KPFM, was introduced as a tool to measure the local contact potential difference between a conducting atomic force microscopy (AFM) tip and the sample, thereby mapping the work function or surface potential of the sample with high spatial resolution. Since its first introduction by Nonnenmacher et al. in 1991 [1], KPFM has been used extensively as a unique method to characterize the nano-scale electronic/electrical properties of metal/semiconductor surfaces and semiconductor devices. Recently, KPFM has also been used to

* Corresponding author. Tel.: +1 858 534 9505; fax: +1 858 534-2063.
E-mail address: sangyeob@ucsd.edu (S. Lee).

0167-5729/$ – see front matter © 2010 Elsevier B.V. All rights reserved.
doi:10.1016/j.surfrep.2010.10.001

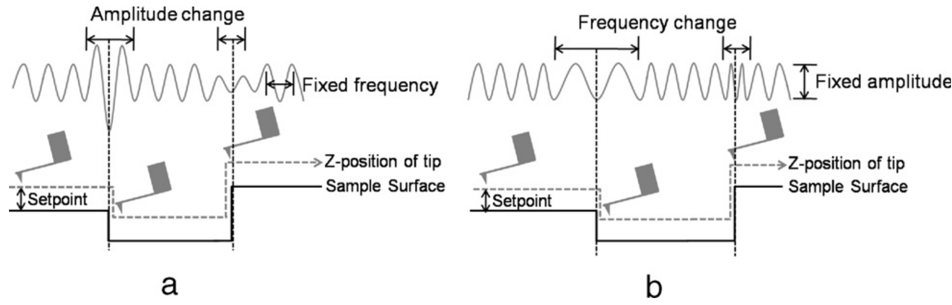

Fig. 1. Schematic depiction of non-contact AFM operation mode: (a) Amplitude modulation mode and (b) Frequency modulation mode. Both AM and FM modes maintain constant tip–sample separation. AM mode uses oscillation amplitude changes as a feedback signal while FM mode uses frequency changes as feedback signal.

study the electrical properties of organic materials/devices [2–4] and biological materials [5,6].

This review presents the principles and theory of KPFM and explores the use of sub-nanometer resolution KPFM to characterize the electrical properties of metal and semiconductor materials/devices.

Since the KPFM experimental is an AFM based apparatus, the basic operational principles and instrumentation of AFM and KPFM are reviewed together. A comparison is made between KPFM and other surface potential or work function measurement tools. Recent reports show that KPFM can be used to image potential distributions on the surface with sub-nanometer resolution, making KPFM the best technique, at present, for characterizing the electrical properties of nanostructures.

KPFM measures a contact potential difference (CPD) between the sample surface and the tip. In high-resolution KPFM, CPD is strongly affected by a short-range force between tip and sample. The CPD associated with the short-range force is specifically referred as the local contact potential difference (LCPD). For the high-resolution KPFM, understanding the fundamental difference between the CPD and the LCPD is critical, as is knowing how the CPD and LCPD correspond to physical properties of the surface.

Applications of KPFM to electrical property analysis of nanostructures are reviewed in the second part. (1) KPFM characterization of the electrical properties of metallic nanostructures is described. KPFM has enabled the experimental determination of quantum size effects on the electronic properties of metallic nanostructures. (2) KPFM has been used to study of electronic properties of semiconductor nanostructures and surfaces. Electronic properties of defects on clean semiconductor surfaces have been investigated using sub-nanometer resolution KPFM. High-resolution KPFM has been successfully applied to the study of a variety of adsorbates and their interaction with semiconductor surfaces. (3) High-resolution KPFM has been used to probe semiconductor devices. A notable application of KPFM is the imaging of operational electrical devices to provide the high-resolution potential profiles. These measurements provide critical, near-atomic scale information on processing induced defects and their effects to the performance of the electrical devices.

2. Principles of scanning Kelvin probe force microscopy

2.1. Basic principle of atomic force microscopy

KPFM is primarily based on the instrumentation of an AFM system. AFM operates in contact, intermediate (tapping), and non-contact modes. In contact mode operation, the AFM tip touches the sample surface, and the tip–sample repulsive force deflects the tip–cantilever. The cantilever deflection is monitored and used as a feedback signal. In intermediate and non-contact mode, the cantilever is externally oscillated at, or close to, its resonance frequency. The tip–sample interaction is altered as the tip–sample distance changes, leading to a change in oscillation amplitude (intermediate mode) and resonance frequency (non-contact mode). These amplitude and frequency changes, with respect to the reference amplitude and frequency, are used as feedback signals to obtain the topography of the sample surface. Therefore, intermediate mode and non-contact mode are referred as amplitude modulation (AM) and frequency modulation (FM) operation, respectively.

In intermediate and non-contact mode AFM, the tip–sample interaction is perturbed by attractive and repulsive forces, causing amplitude or frequency changes in the oscillation of the AFM tip, as illustrated schematically in Fig. 1. In AM mode AFM, changes in the oscillation amplitude provide the feedback signal for imaging. As seen in Fig. 1(a), the amplitude of oscillation increases as the tip–sample distance increases, due to the decrease of tip–sample interaction. The amplitude change is monitored and regulated by a feedback system to keep the tip–sample distance constant at a pre-determined set-point. The dependence of amplitude change on the tip–sample interaction can be described analytically, based on the harmonic oscillator model, and the amplitude change is generally accepted to be dependent on the force between the tip and sample. Therefore, AM mode measurements represent the direct force between the tip and sample [7,8].

In FM mode AFM, changes in the oscillation frequency provide information about tip–sample interactions. The cantilever oscillation frequency changes due to the tip–sample distance variation, as illustrated in Fig. 1(b). A feedback system regulates the frequency change to keep the set-point frequency constant, allowing the topography of the sample surface to be acquired. The changes in oscillation frequency are dependent on the force gradient between tip and sample when the restoring force of the cantilever that is associated with tip oscillating energy is large compared to the interaction force between the tip and sample surface [8,9]. Therefore, the FM mode AFM detects the force gradient rather than force itself, a factor enabling FM mode AFM to have higher spatial resolution than AM mode AFM.

AFM resolution is dependent on the quality factor (Q) of the vibrating cantilever, a measure of the energy loss of the oscillation [7]. Q is defined as the ratio between resonant frequency (f_0) and frequency change (Δf) at full-width-half-maximum:

$$Q = \frac{f_0}{\Delta f}. \tag{2.1}$$

In air, the typical Q of a cantilever, with a resonant frequency of 300 kHz, is approximately 100. The Q in ultra-high vacuum (UHV) is approximately 50,000, 500 times the Q in air [8]. An expression for the minimum detectable force (δF_{min}) by an AFM is:

$$\delta F_{min} = \sqrt{\frac{2k_L k_B TB}{\omega_0 Q \left\langle z_{osc}^2 \right\rangle}}, \tag{2.2}$$

where k_L is the force constant of the cantilever, k_BT is the thermal energy at the ambient temperature, B is the measurement bandwidth, ω_0 is the resonant frequency of tip, and $\left\langle z_{OSC}^2 \right\rangle$ is the

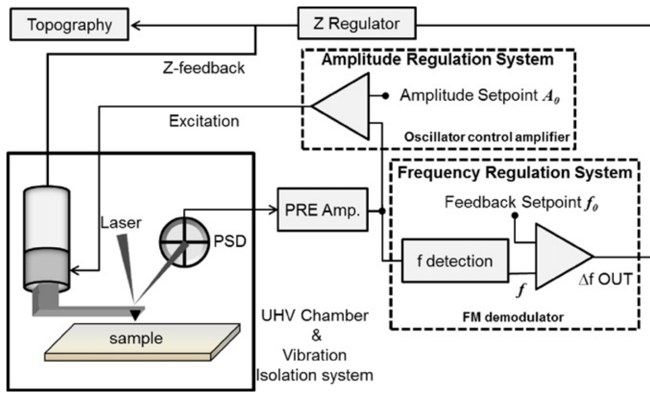

Fig. 2. Block diagram of FM mode AFM system operated in UHV. The piezo scanner and the laser/PSD are enclosed in a UHV chamber system. The laser signal is amplified through the pre-amp and fed into two feedback systems for the amplitude and frequency regulation systems. The amplitude is set to a pre-determined set-point A_0. The frequency shift (Δf) is kept constant to acquire topographic images of the sample surface.

mean-square amplitude of the driven cantilever vibration [9]. Since the Q in UHV is 500 times greater than Q in air, the sensitivity of the AFM system can be 20–25 times greater in UHV than air. Therefore, it is desirable to operate the AFM in UHV to achieve high-resolution. However, it is not desirable to operate AM mode AFM in UHV, since the amplitude change response occurs slowly with tip–sample interaction due to the increased Q in UHV. The time scale of amplitude change in AM mode (τ_{AM}) is given by [9]:

$$\tau_{AM} \approx \frac{2Q}{f_0}. \tag{2.3}$$

The time scale of the amplitude change is linearly dependent on Q in AM mode AFM. In contrast, the frequency change time response in FM mode AFM does not depend on Q. The time scale of frequency change in FM mode (τ_{FM}) is given by [9]:

$$\tau_{FM} \approx \frac{1}{f_0}. \tag{2.4}$$

Therefore, FM mode AFM operated in UHV, with increased Q, results in high-resolution AFM imaging.

An AFM system is typically composed of tip–sample interaction monitoring (laser and position sensitive detectors) and feedback systems. Fig. 2 shows the schematic of an FM mode AFM working in a UHV environment. The amplitude regulation feedback system and the frequency regulation feedback system are the two feedback loops in an FM mode AFM system. The amplitude regulation feedback system keeps the amplitude of the AFM tip oscillation constant, while the frequency regulation feedback system maintains the frequency shift (the difference between the tip oscillation frequency and the set-point frequency) constant by adjusting the z-position of the AFM tip. The tip oscillation is monitored by the laser beam movement by a position sensitive detector (PSD). A pre-amp amplifies the PSD signal. The amplitude signal of the tip oscillation feeds into the amplitude regulation system. The amplitude regulation system generally consists of a positive feedback amplifier, a band-pass filter, and a phase shifter to detect an amplitude peak and to generate an excitation signal for cantilever oscillation. Concurrently, the FM demodulator (phase-locked-loop) measures the oscillation frequency (f) and compares f with the pre-defined set-frequency f_0 [10]. The error signal $f - f_0$ feeds into the z regulator, which controls the z-position of the tip to maintain a constant tip–sample interaction by minimizing $f - f_0$.

2.2. Kelvin probe force microcopy

2.2.1. Fundamentals of KPFM

The KPFM measures CPD between a conducting AFM tip and a sample. The CPD (V_{CPD}) between the tip and sample is defined as:

$$V_{CPD} = \frac{\phi_{tip} - \phi_{sample}}{-e}, \tag{2.5}$$

where ϕ_{sample} and ϕ_{tip} are the work functions of the sample and tip, and e is the electronic charge. When an AFM tip is brought close to the sample surface, an electrical force is generated between the tip and sample surface, due to the differences in their Fermi energy levels. Fig. 3 shows the energy level diagram of the tip and sample surface when ϕ_{sample} and ϕ_{tip} are different. Fig. 3(a) depicts the energy levels of the tip and sample surface when separated by a distance d and not electrically connected (note, the vacuum levels are aligned but Fermi energy levels are different). Equilibrium requires Fermi levels to line-up at steady state, if the tip and sample surface are close enough for electron tunneling. Upon electrical contact, the Fermi levels will align through electron current flow, and the system will reach an equilibrium state, Fig. 3(b). The tip and sample surface will be charged, and an apparent V_{CPD} will form (note, the Fermi energy levels are aligned but vacuum energy levels are no longer the same, and a V_{CPD} between the tip and sample has formed). An electrical force acts on the contact area, due to the V_{CPD}. As shown in Fig. 3(c), this force can be nullified. If an applied external bias (V_{DC}) has the same magnitude as the V_{CPD} with opposite direction, the applied voltage eliminates the surface charge in the contact area. The amount of applied external bias (V_{DC}) that nullifies the electrical force due to the V_{CPD} is equal to the work function difference between the tip and sample; therefore,

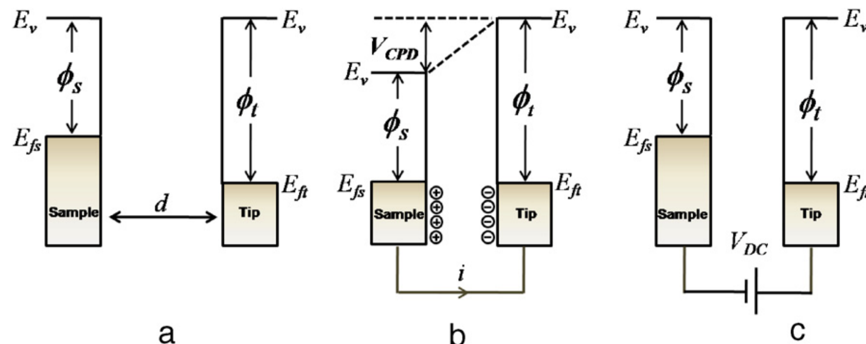

Fig. 3. Electronic energy levels of the sample and AFM tip for three cases: (a) tip and sample are separated by distance d with no electrical contact, (b) tip and sample are in electrical contact, and (c) external bias (V_{dc}) is applied between tip and sample to nullify the CPD and, therefore, the tip–sample electrical force. E_v is the vacuum energy level. E_{fs} and E_{ft} are Fermi energy levels of the sample and tip, respectively.

the work function of the sample can be calculated when the tip work function is known.

By applying an AC voltage (V_{AC}) plus a DC voltage (V_{DC}) to the AFM tip, KPFM measures the work function of the sample. V_{AC} generates oscillating electrical forces between the AFM tip and sample surface, and V_{DC} nullifies the oscillating electrical forces that originated from CPD between tip and sample surface. The electrostatic force (F_{es}) between the AFM tip and sample is given by:

$$F_{es}(z) = -\frac{1}{2}\Delta V^2 \frac{dC(z)}{dz}, \tag{2.6}$$

where z is the direction normal to the sample surface, ΔV is the potential difference between V_{CPD} and the voltage applied to the AFM tip, and dC/dz is the gradient of the capacitance between tip and sample surface. When $V_{AC}\sin(\omega t) + V_{DC}$ is applied to the AFM tip, the voltage difference ΔV will be:

$$\Delta V = V_{tip} \pm V_{CPD} = (V_{DC} \pm V_{CPD}) + V_{AC}\sin(\omega t). \tag{2.7}$$

Note that the $\pm$ sign depends whether the bias (V_{DC}) is applied to the sample (+) or the tip (−) [11]. Substituting Eq. (2.7) in Eq. (2.6) gives the expression of the electrostatic force applied to the AFM tip:

$$F_{es}(z,t) = -\frac{1}{2}\frac{\partial C(z)}{\partial z}\left[(V_{DC} \pm V_{CPD}) + V_{ac}\sin(\omega t)\right]^2. \tag{2.8}$$

This equation can be divided into three parts:

$$F_{DC} = -\frac{\partial C(z)}{\partial z}\left[\frac{1}{2}(V_{DC} \pm V_{CPD})^2\right] \tag{2.9}$$

$$F_{\omega} = -\frac{\partial C(z)}{\partial z}(V_{DC} \pm V_{CPD})\, V_{AC}\sin(\omega t) \tag{2.10}$$

$$F_{2\omega} = \frac{\partial C(z)}{\partial z}\frac{1}{4}V_{AC}^2\left[\cos(2\omega t) - 1\right]. \tag{2.11}$$

F_{DC} (Eq. (2.9)) results in a static deflection of the AFM tip. F_{ω} with frequency ω (Eq. (2.10)) is used to measure the V_{CPD}, and $F_{2\omega}$ can be used for capacitance microscopy [12]. When electrostatic forces are applied to the tip by V_{AC} with V_{DC}, additional oscillating components (due to the electrical force) will be superimposed to the mechanical oscillation of the AFM tip. A lock-in amplifier is employed to measure the V_{CPD}, to extract the electrical force component with frequency ω (F_{ω}), a function of V_{CPD} and V_{AC}. The output signal of the lock-in amplifier is directly proportional to the difference between V_{CPD} and V_{DC}. The V_{CPD} value can be measured by applying V_{DC} to the AFM tip, such that the output signal of the lock-in amplifier is nullified and F_{ω} equals zero. Subsequently, the value of V_{DC} is acquired for each point on the sample surface, composing a map of the work function or surface potential of the whole sample surface area.

Eq. (2.8) is derived from the capacitive energy between two parallel metal plates, and the equation is valid for CPD measurements on metallic surfaces. The space-charge-layer (SCL) on the surface of a semiconductor is well-known, and the effect of the SCL has to be considered when measuring CPD on a semiconductor surface. Hudlet et al. analyzed the electrostatic force in a metallic AFM tip/metallic surface and a metallic AFM tip/semiconductor surface [13]. In the case of a semiconductor surface, F_{ω} is derived as:

$$F_{\omega} = -\frac{Q_s}{\varepsilon_0}\frac{C_I C_D}{C_I + C_D}V_{AC}\sin(\omega t), \tag{2.12}$$

where Q_s is total charge near the semiconductor surface due to the surface potential of the semiconductor, ε_0 is the dielectric constant, C_I is the capacitance associated with V_{ac} and the air gap between tip and sample, and C_D is the capacitance associated with V_{ac} and SCL in the semiconductor. For a semiconductor surface, the measured CPD is related to the surface potential, which differs from the work function of semiconductor materials, due to the SCL near the semiconductor surface.

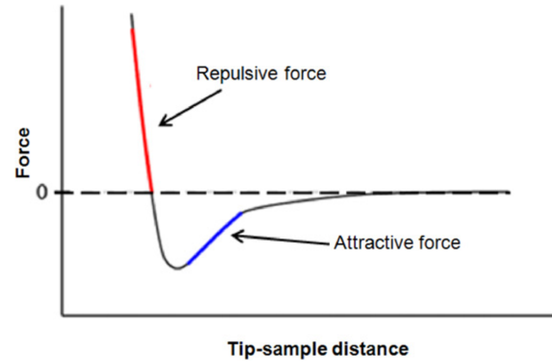

Fig. 4. A typical inter-atomic force vs. distance curve. The force gradient (derivative of curve) is limited to the short-range in tip–sample distance, while the force is long-ranged compared to the force gradient.

2.2.2. KPFM operational mode: FM and AM mode

As previously described, AFM can detect atomic forces by AM or FM mode. The electrostatic force F_{ω} can also be detected either by AM or FM mode in KPFM. AM mode KPFM measures F_{ω} directly from the amplitude of the cantilever oscillation at ω induced by V_{CPD} and V_{AC}. V_{DC} is applied to the AFM tip to nullify the measured amplitude, thereby measuring V_{CPD}. In FM mode KPFM, F_{ω} is detected by the frequency shift at ω, and V_{DC} is applied to the AFM tip to nullify the frequency shift, thereby measuring V_{CPD}.

KPFM measures topography concurrently with V_{CPD}, using an AFM tip. A method to separate the topographical signal from the V_{CPD} measurement is required. In the KPFM experimental setup, the V_{AC} is usually modulated at a frequency higher than the bandwidth of the topography feedback system to prevent cross-talk between topography and CPD measurement. In AM mode KPFM, topography is measured by the oscillation at the first resonance frequency of the AFM tip, and V_{CPD} is measured by the amplitude of the oscillation at the second resonance frequency of the AFM tip. A mechanically vibrated cantilever generally has several resonance peaks in the oscillation amplitude–frequency spectrum. The second resonance peak normally has a broader peak than the first resonance frequency peak. The amplitude of the second resonance peak is usually less than one-third of the first resonance frequency peak, and the frequency of the second resonance peak is typically 6 times the first resonance frequency [14]. V_{AC} is tuned to the second resonance frequency to excite the AFM tip by electrical force, while the first resonance frequency is assigned for the tip height control. Using these techniques, the topography and the V_{CPD} signal can be separated. Conversely, in FM mode KPFM, the AFM tip is mechanically excited at the first resonance frequency. V_{AC} induces a modulation of the electrostatic force, which is detected by the superimposed oscillation at the frequency variation of the mechanical oscillation of the AFM tip, leading to the separation of topography and V_{CPD} signal.

The spatial resolution of measuring V_{CPD} in FM mode KPFM is higher than in AM mode KPFM. Similar to the AM and FM mode AFM, the AM mode KPFM directly detects the electrostatic force by the oscillation of the cantilever, but the FM mode KPFM detects the electrostatic force gradient by the frequency shift of the cantilever oscillation, which contributes to greater spatial resolution [14,15]. However, the detection range of the force gradient is shorter-ranged than the force itself, which is explained by the inter-atomic force–distance curve.

Fig. 4 shows the typical force–distance curve. In the attractive force regime, the force gradient (the derivative of the force–distance curve) becomes larger when the inter-atomic distance is small. As the inter-atomic distance increases, the force gradient becomes insignificant. Therefore, the detection of force

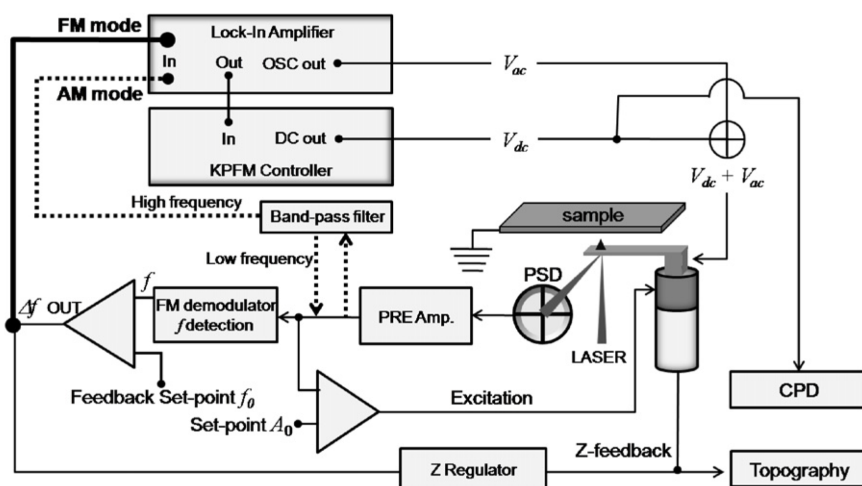

Fig. 5. Schematic diagram of KPFM system showing AM and FM mode. Lower part of the diagram is an FM mode AFM system for topography imaging and upper part is a KPFM system for CPD measurement.

Table 1
Typical spatial and energy resolution of FM and AM mode KPFM.

KPFM mode	Spatial resolution	Energy resolution (meV)
FM	Possibly sub-nanometer resolution depending on tip apex	10–20
AM	Typically 25 nm (sub-nanometer resolution also possible depending on sample)	5

gradient mainly takes place at the end of the AFM tip. Consequently, the detection of electrostatic force is considered long-range detection, whereas the detection of electrostatic force gradient is short-range detection. The electrostatic interaction takes place mainly between the tip apex and sample surface in the FM mode KPFM. The spatial resolution is approximately equal to the dimension of the tip apex in the FM mode KPFM. However, the electrostatic interaction from the sample includes both the tip and the cantilever in AM mode KPFM due to the long-range detection scheme. As a result, the spatial resolution of AM mode KPFM is reduced by an averaging effect between the tip and cantilever.

Although FM mode KPFM is generally considered to have better spatial resolution than AM mode, it has been demonstrated that AM mode can also show the atomic-scale resolution in KPFM images [16]. The aforementioned comparison of spatial resolution of FM and AM mode KPFM includes only long-range electrostatic interaction. However, recent theoretical studies on the limitation of FM and AM mode KPFM suggested that the short-range interaction becomes more significant in atomic-scale KPFM and both FM and AM mode KPFM in the sub-nanometer regime have the same limitation in spatial resolution (see Section 2.2.5) [17].

The energy resolution of measurements of V_{CPD} in AM mode KPFM is higher than in FM mode KPFM. AM mode KPFM measures the V_{CPD} from the resonance peak of the oscillating cantilever greatly enhancing the signal-to-noise ratio [14,18]. Conversely, FM mode KPFM detects the V_{CPD} through an FM demodulator [14], and additional noise is generated, when the signal passes through the FM demodulator. Consequently, the energy resolution of AM mode KPFM is superior, due to the high signal-to-noise ratio compared to FM mode KPFM. The typical spatial and energy resolutions of V_{CPD} measurement by FM and AM mode KPFM are listed in Table 1.

2.2.3. KPFM instrumentation and preparation of conducting AFM tip

Fig. 5 shows the schematic diagram of a KPFM experimental apparatus. The lower part shows the FM mode AFM system for topography measurement, and the upper part shows the components for CPD mapping, including the KPFM controller and lock-in amplifier. The dashed line and bold straight line in the diagram show the AM and FM mode KPFM configurations. V_{ac} is applied to the tip from the lock-in amplifier reference signal voltage output (OSC out). In FM mode, the frequency shift signal (Δf) is split into two; one goes to the z regulator for topographic imaging, and the other is fed into the lock-in amplifier. The lock-in amplifier extracts the signal with the same frequency as V_{ac} and feeds the signal into the KPFM controller. The KPFM controller maintains feedback to nullify the lock-in output signal, by applying V_{dc} to the tip. In AM mode, V_{ac} with the same frequency as the second resonant peak of tip oscillation is applied to the AFM tip to excite the tip with electrical force. The amplitude of tip oscillation has two components; low frequency (the first resonance peak) tuned by mechanical oscillation and high frequency (the second resonance peak) tuned by V_{ac}. A band-pass filter filters the low and high frequency signals. The low frequency signal is used for topography regulation. The high frequency signal feeds directly into the lock-in amplifier. The KPFM controller measures CPD using the second resonance frequency component.

The preparation of atomically sharp and conducting AFM tips is critical for high-resolution KPFM. An AFM tip can be prepared for high-resolution KPFM using any of several methods. (a) The most common method is to take a commercially available heavily doped Si cantilever and use heat treatment followed by Ar^+ bombardment to remove the native oxide layer and other contaminants [19–21]. These tips routinely produce high-resolution images, but are more likely to pick up surface atoms, altering the work function of the tip. (b) Some commercially available tips, for example, Pt/Ir-coated Si cantilevers, can produce sub-nanometer resolution KPFM images [16,22]. The commercial Pt/Ir-coated tips do not require substantial tip preparation, but yield lower spatial resolution. (c) HF wet etching of Si tips followed by a high temperature annealing has also been successful for high-resolution KPFM imaging [23]. Etching Si tips is an alternative method to ion bombardment to remove the native oxide. (d) The coating of Si cantilevers with a very thin Au or Cr layer (typically a few nm thick) also produces high-resolution KPFM images [24,25]. Cr-coated tips are less reactive so that they have a more stable tip work function. Obtaining the best spatial resolution requires optimization of the tip coating film thickness. (e) UHV field emission tip cracking can produce sub-nanometer resolution. A tungsten filament is positioned close to the cantilever, and a high voltage is applied between the tungsten filament and the AFM tip. Electrons tunneling from the filament to the tip remove the native

Table 2
Comparison of Kelvin probe force microscopy, Kelvin probe method, photoemission spectroscopy, and scanning electron microscopy to measure the surface potential.

Method	Description	Energy resolution	Spatial resolution
KPFM	Measuring local CPD of the sample surface	5–20 meV	Better than 10 nm [24]
KP	Measuring CPD of the whole sample surface	1 meV	Averaging a whole sample surface
PES	Measuring energy spectroscopy of the whole sample surface	20 meV [29]	Better than 100 nm [29]
SEM	Measuring electron beam induced current to map the surface potential	Not a quantitative method	Better than 70 nm [30]

oxide. (f) The simplest method to make a conducting silicon AFM tip is gently touching the AFM tip end into the sample surface, removing the native oxide [26,27].

2.2.4. Comparison of KPFM to other surface potential measurement systems

The surface potential or work function of a sample can also be measured by various techniques such as Kelvin probe (KP), photoelectron spectroscopy (PES), and scanning electron microscopy (SEM) with electron beam induced current (EBIC) analysis. Similar to KPFM, the KP also measures the CPD between the probe and sample surface. The working principle of KPFM and the KP are similar, but the KP is an averaging method including the CPD values of the whole sample area which does not provide a map of the CPD on the sample surface. PES measures the energy of photo-stimulated electrons emitted from a sample surface. Angle resolved high resolution PES can be used to determine the electronic band structure of the sample. SEM can also resolve the local electronic structure of the semiconductor sample surface by measuring EBIC [28].

When semiconductor sample surfaces are bombarded by energetic electrons (typically several keV), electron–hole pairs are generated. The generated electrons and holes are free to move in a sample. In the absence of any local electric fields, these electrons and holes move randomly and typically recombine. When local electric fields exist within a semiconductor sample, the local electric fields can separate the electrons and holes, and EBIC can flow throughout the sample. The EBIC is linearly dependent on the local electric field on the sample surface. The surface potential of a sample (as a function of the local electric field) is mapped by monitoring the EBIC signal during the scanning of the electron beam over the sample surface.

The spatial resolution of KPFM is higher than of the PES and EBIC methods. The sensitivity of KPFM in measuring either the surface potential or work function is comparable to PES but less than KP. Typically, laboratory scale PES has been used to measure the electronic band structures of the whole sample surface. The spatial resolution has improved gradually to 3 μm, due to improvements in the photon source and electron energy analyzer. When synchrotron radiation sources are used for PES, a spatial resolution better than 100 nm is possible [29].

The spatial resolution of EBIC technique can be 70 nm [30]. However, the EBIC technique has some disadvantages in measuring the surface potential of samples. The technique can only be applied to a semiconductor sample, since EBIC measures the current generated from electron–hole pairs. In addition, the absolute surface potential is difficult to quantify, since the correlation between EBIC and surface potential values is not physically defined. Table 2 summarizes the spatial and energy resolution of KPFM, KP, PES, and SEM.

Although KPFM has superior spatial resolution with relatively high energy sensitivity compared to other measurement techniques, KPFM has some disadvantages in measuring the absolute surface potential or work function of a sample. First, the absolute measurement of surface potential using KPFM requires measurement of the work function of the probe. This requires the calibration of KPFM probe on a sample with a well-defined work function. Therefore, two measurements are needed, one on the reference surface and one on the sample. The necessary exchange of the two samples under the KPFM probe decreases the accuracy of the measurement [31]. PES and SEM do not require calibration of the probe when measuring the surface potential or capacitance of a sample surface.

Second, KPFM can only measure the molecularly averaged surface potential changes when a semiconductor sample surface contains absorbents. KPFM measurements cannot distinguish the contributions of surface band bending and surface dipoles created by absorbents from the semiconductor surface [31,32].

PES techniques can provide the entire spectral distribution of the surface potential allowing determination of the complete electronic band structure of a sample surface. By comparing PES measurements of the electronic band structures of a clean surface and a surface with absorbents, band bending and surface dipole contributions can be independently determined [31–33].

Third, an abrupt topographic height change can disrupt the accurate measurement of KPFM. KPFM requires keeping the tip–sample distance constant during measurement to avoid the contribution of capacitance gradients (see Eq. (2.6)) to the surface potential (see the Eq. (2.10)) [1,14,18,34]. When a sudden change in a topographic height during KPFM measurement occurs, the capacitance gradient term in Eq. (2.10) can change. The change of capacitance gradient can contribute to the electrical force between the tip and sample. Consequently, the measured surface potential value does not always represent of the contact potential between the tip and sample. In contrast, the surface potential measured by KP, PES and SEM does not depend on the tip–sample distance.

Fourth, KPFM requires a relatively long time to acquire an image of a sample surface potential (typically one or two hours). KPFM measures the surface topography and potential at the same time using one AFM tip. When the tip is scanned on a sample surface at high speed, severe cross-talk between topographic and surface potential signals can be generated [14]. Consequently, the scan-bandwidth of the topography and surface potential regulation is limited to avoid the cross-talk. High resolution PES is also very slow.

2.2.5. High-resolution KPFM: concept of LCPD

In the past decade, atomic-resolution KPFM was demonstrated on a variety of surfaces, including semiconductors and ionic solids. The CPD in Eq. (2.5) is based on the capacitive force between two macroscopic parallel metallic electrodes, which, do not have lateral electrostatic force distributions at the atomic-scale. In atomically resolved KPFM, the measured CPD is defined as LCPD, which depends on the electrostatic interaction on the atomic-scale. The LCPD is based on the Wandelt's concept of a local work function, which illustrates the short-ranged (along the direction normal to surface) atomic scale variation of work function on metal surfaces [35]. Similar to the local work function concept, atomic-scale KPFM measurements of the total electrostatic force includes a new term (a bias dependent short-range force), which induces the atomic LCPD contrast. All published theories of LCPD attribute the atomic-scale contrast of CPD to a short-range force, due to the microscopic interaction between the apex of the tip and surface atoms. For ionic solids, the tip–sample interaction resulting in atomic contrast is the ionic bonding force (dipole interactions)

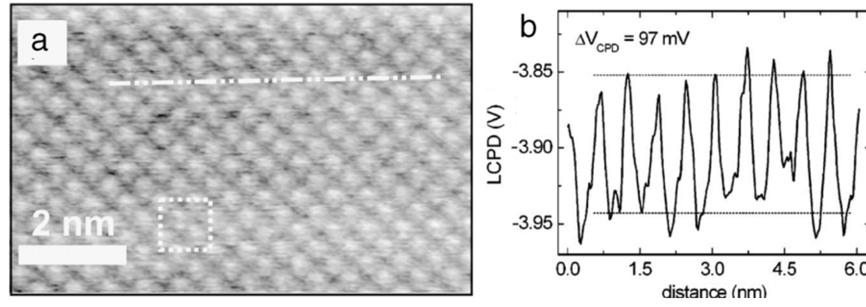

Fig. 6. Atomic resolution KPFM image of KBr(001) surface. (a) CPD image of KBr(001) surface measured by AM mode KPFM in UHV. (b) Line trace of CPD indicated by the dash line in (a). 97 mV LCPD is clearly observed between K^+ and Br^-. The dashed box indicates unit cell.
Source: Adapted from [21].

between the surface atom and the tip apex atom. In semiconductor surfaces, the short-range force is attributed to a covalent bonding interaction. The origin of the short-range force is highly dependent on the system. In different systems, different short-range forces can dominate over the other forces. The dominant short-range force is minimized by applying a potential to the tip, causing the LCPD contrast.

2.2.5.1. LCPD in ionic solids. Bocquet et al. reported atomic-resolution KPFM results on ionic solids such as KBr(001) [21]. Fig. 6 shows the atomically resolved CPD images of KBr(001) surface. The LCPD between K^+ and Br^- shows a clear 97 mV difference. Bocquet et al. also developed an analytical model describing the short-range electrostatic force between a conducting AFM tip and an ionic crystal, and showed the short-range electrostatic interaction between the microscopic tip-end and the local charge distribution on the ionic crystal surface can account for the LCPD.

Based on the analytical model developed by Bocquet et al., Nony et al. also suggested an analytical model of short-range electrostatic forces which creates the LCPD contrast on ionic crystals by AM and FM mode KPFM [17]. An interaction of atoms on the tip apex with the surface provides a lateral force distribution at the atomic scale. However, the LCPD has a dependence on the tip geometry, tip–sample distance, and bias between tip and sample.

The short-range electrostatic force is divided into two separate terms. $F^{(1)}_{m\mu}$ represents the interaction between the microscopic tip apex (which acts as a capacitor with the sample surface) and the sample counter electrode. $F^{(2)}_{\mu}$ represents the force between the mesoscopic tip apex with the surface charge density caused by applied bias and the sample. The expression for the total short-range electrostatic force is [17]:

$$\begin{aligned} F_{es}(V_{applied}, z) &= F^{(1)}_{m\mu} + F^{(2)}_{\mu} \\ &= C_1(V_{applied}(t) - V_{CPD})\mathrm{e}^{-\alpha z} \\ &\quad + [C_0 + C_2(V_{applied}(t) - V_{CPD})^2]\mathrm{e}^{-2\alpha z}, \end{aligned} \tag{2.13}$$

where $\alpha = 2\sqrt{2\pi}/a$ and a is the lattice constant of sample surface. The coefficients are defined as:

$$C_0 = -\frac{2R^2q^2}{\varepsilon_0 a^4}A^{(2)}\mathrm{e}^{-2\alpha R_a} \tag{2.14}$$

$$C_1 = -\frac{6R_a^2 q\tilde{\varepsilon}_d}{a^2 R}D^{(1)}\mathrm{e}^{-\alpha R_a}\left[\cos\left(\frac{4\pi x_0}{a\sqrt{2}}\right) + \cos\left(\frac{4\pi y_0}{a\sqrt{2}}\right)\right] \tag{2.15}$$

$$C_2 = C_0\left(\frac{4\pi \chi_d}{aqR}\right)^2, \tag{2.16}$$

where ε_0 is vacuum dielectric permittivity, $\tilde{\varepsilon}_d$ is the effective dielectric permittivity (for KBr $\tilde{\varepsilon}_d = 4.38$) and χ_d is the dielectric susceptibility (for KBr $\chi_d = 9 \times 10^{-39}$ F m^2). R (typically larger than 5 nm) is the mesoscopic tip radius, and R_a is the microscopic tip apex radius. $A^{(2)}$ (typically −8) and $D^{(1)}$ (typically −15) are integral coefficients [21]. The relative positions of the anion and the cation are $x_0 = y_0 = 0$ and $x_0 = y_0 = a\sqrt{2}/4$, respectively. The coefficient C_1 contains the spatial components (x_0 and y_0), whereas C_0 and C_2 are not related to spatial variation. Therefore, $F^{(1)}_{m\mu}$ contributes to the atomic LCPD contrast, and $F^{(2)}_{\mu}$ is a static offset.

Based on the local electrostatic force caused by LCPD, Nony et al. also proposed an analytical model correlating the external bias and LCPD in FM and AM mode KPFM, using a nonlinear equation of motion [17]. The force equation, including the short-range interaction, translates to an additional term in the measured CPD. The analytical expression for the measured LCPD in FM and AM mode KPFM has been derived as follows [17]:

$$V_{LCPD} = V_{CPD} - \frac{C_1}{2C_2}\frac{a_n}{b_n}\mathrm{e}^{\alpha z_{min}}, \tag{2.17}$$

where a_n and b_n are Fourier coefficients and z_{min} is the minimum tip–sample distance. It should be noted that by only including the short-range electrostatic forces that LCPD diverges at large tip–sample separations. The order of the Fourier coefficients is dependent on the mode of operation of the KPFM. The coefficients are zero-order ($a_0 = 0.1155$ and $b_0 = 0.0724$) for AM mode. The coefficients are first-order ($a_1 = 0.1080$ and $b_1 = 0.0766$) for FM mode. The difference in coefficients is responsible for the variation in the measurements between AM and FM mode KPFM. The difference between AM and FM is expected to be small because the a to b ratios are nearly the same. Nony et al. also extend this model to include the long-range electrostatic force. Experimentally, long-range electrostatic forces accompany the short-range electrostatic forces.

The full force expression, including both the short-range and long-range electrostatic interaction, is expressed as [17]:

$$F_{es}(V_{applied}, z) = F^{(1)}_{m\mu} + F^{(2)}_{\mu} + F_M, \tag{2.18}$$

where F_M is the macroscopic electrostatic force in terms of z (the direction normal to sample surface). F_M is the macroscopic electrostatic force [17]:

$$F_M(V_{applied}, z) = -\frac{1}{2}\frac{S\varepsilon_0\tilde{\varepsilon}_d^2}{(z_M+z)^2}\left(V_{applied} - \frac{CPD}{e}\right)^2, \tag{2.19}$$

where S is the surface area of the tip and z_M is the height of the tip, with approximate values of $S = 1$ mm^2 and $z_M = 5$ mm. ε_0 and ε_d are the dielectric constant of vacuum and the relative dielectric constant.

The compensated potential difference required to minimize the total electrostatic force, including the macroscopic long-range and the short-range electrostatic forces for FM mode KPFM is [17]:

$$V^{(c)}_{DC} = V_{CPD} - \frac{C_1 a_1 \mathrm{e}^{-\alpha z_{min}}}{2C_2 b_1 \mathrm{e}^{-2\alpha z_{min}} + 2\pi\, S\varepsilon_0\tilde{\varepsilon}_d^2 A_0 z_M^3}, \tag{2.20}$$

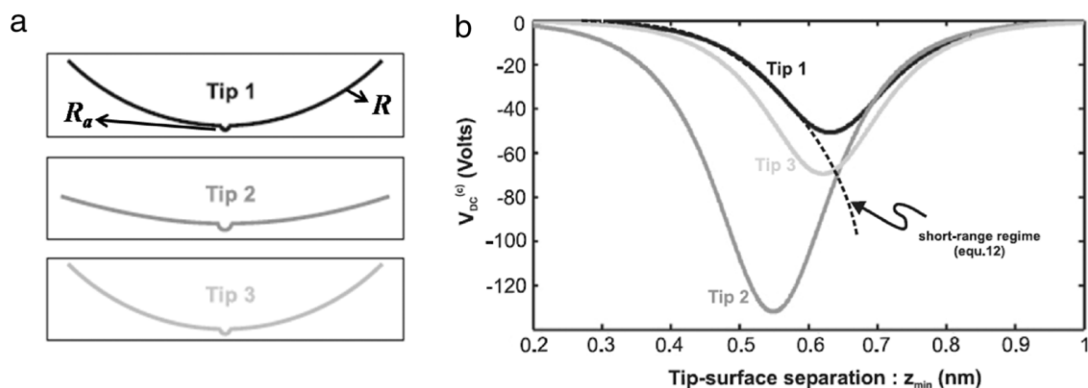

Fig. 7. Compensated potential difference vs. tip–sample distance. (a) Models of the three tips used for the analytical and numerical calculation. The parameters (R, R_a) in Å are: tip 1 (50, 1); tip 2 (120, 1.5); tip 3 (50, 1.1). R (typically larger than 5nm) is the mesoscopic tip radius, and R_a is the microscopic tip apex radius. (b) The total potential difference ($V_{DC}^{(c)}$) for tip 1 (black), tip 2 (dark grey) and tip 3 (light grey). The dotted line indicated the short-range regime. The curves indicate an optimal tip–sample distance for LCPD contrast.
Source: Adapted from [17].

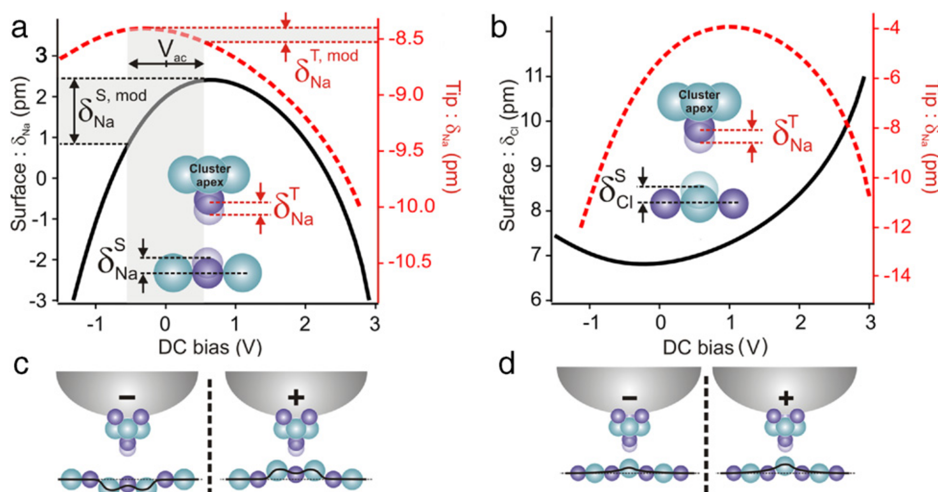

Fig. 8. Atomic movement of the tip and sample vs. position and applied bias. (a) Movement vs. dc bias when tip positioned 0.45 nm above the Na^+ surface atom. The solid line is the surface movement δ_{Na}^{T}. The dashed line is the tip displacement δ_{Na}^{S}, where the positive movement is up towards the tip. (b) Movement vs. dc bias when tip positioned 0.45 nm above the Cl^- surface atom. The solid line is the surface displacement δ_{Cl}^{T}. The dashed line is the tip displacement δ_{Cl}^{S}. (c) Model illustrating the atomic displacement for positive and negative tip bias when positioned above a surface Na^+ atom or (d) Cl^- atom.
Source: Adapted from [36].

where A_0 is the vibration amplitude of the cantilever, and $\alpha = 2\sqrt{2}\pi/a$ with a being the lattice constant of the crystal. The compensated potential difference is the theoretical value applied to minimize the force accounting for tip geometry and tip–sample distance. By including the long-range electrostatic forces, the divergence observed in Eq. (2.17) disappears. Fig. 7 shows the compensated potential difference for the three different tip geometries. The curves indicate a resonant behavior between the short-range and long-range regimes. The resonance behavior implies an optimal tip–sample distance, which amplifies the forces responsible for the LCPD contrast. An optimal tip–sample distance is observed experimentally [16,19,23,36].

Using an atomic force microscope simulator, Nony et al. showed details of the interaction behavior of the cluster of atoms (microscopic apex) and the surface atoms of NaCl (001) [36]. The simulated microscopic apex used a Na atom as the apex atom. Both the tip apex atom and surface atoms could be spatially perturbed depending on tip position and biasing. With the tip positioned above a Na^+ surface atom at zero bias, the Na atom on the tip moves 0.085 Å towards the surface and the surface Na^+ atom moves 0.02 Å towards the tip. With tip positioned above the Cl^- surface atom, the Na atom on the tip moves 0.06 Å towards the surface and the Cl^- surface atom moves 0.07 Å towards the tip. Fig. 8 shows the atomic motion dependence on tip biasing. The movement of the atoms is caused by the equilibrium of two

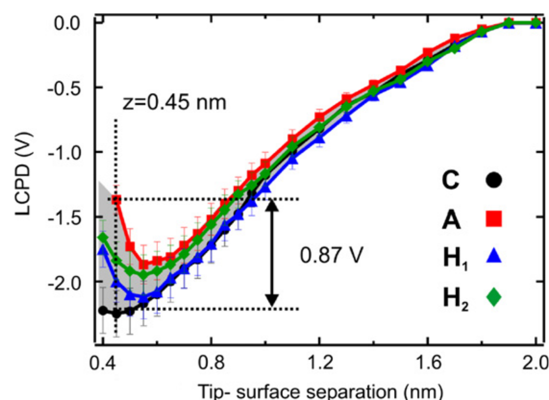

Fig. 9. Calculated LCPD vs. Z spectroscopy curves. Four different sites on NaCl surface (C: on top of Na^+, A: on top of Cl^-, H_1 and H_2: hollow sites between Na^+ and Cl^-). The distance dependence on the difference in the measured LCPD indicates an optimal tip–sample distance for LCPD contrast.
Source: Adapted from [36].

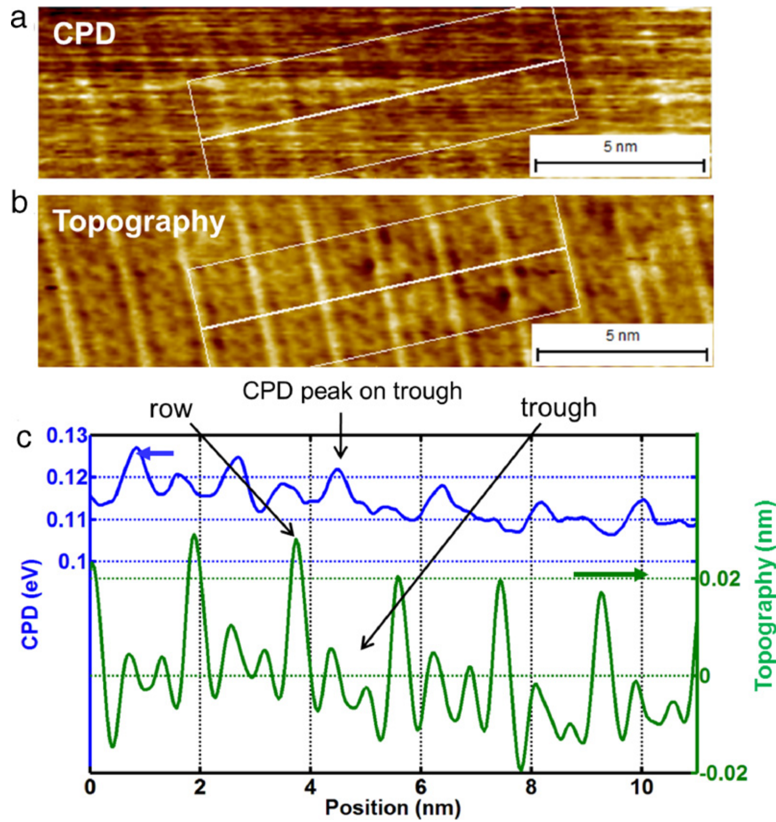

Fig. 10. Sub-nanometer resolution FM mode KPFM on InAs(001)-(4 × 2) surface. (a) LCPD and (b) topography of InAs(001)-(4 × 2) surface. (c) Average line profiles of topography and LCPD. The line profiles are averaged over the area indicated by white lines on (a) and (b). (Experimental results performed by authors.)

separate interactions, the chemical interaction of the apex tip with the surface and the electrostatic interaction of the tip with the local surface area. Calculated force-z spectroscopy at four different positions on the NaCl surface illustrates the tip–sample dependence on the LCPD contrast. Fig. 9 shows the calculated dependence of the tip–sample distance on the contrast between different positions on the NaCl surface. The force-z curves for position A and C have a drastic change around 0.4 nm tip–sample separation. The curves indicate a separation of 0.45 nm generates the contrast of 0.87 V. The existence of an optimal tip–sample separation is consistent with the previous discussed experiments for KBr.

For ionic solids, the measured LCPD is a combination of short-range and long-range electrostatic interactions. The short-range electrostatic interactions appear to originate from the ionic interactions of the tip apex with the surface position directly under the tip and the microscopic electrostatic influence of the tip on the ionic surface. Theoretical calculations support the tip conditions needed to achieve LCPD contrast includes the microscopic apex radius, the mesoscopic tip radius, and the tip–sample distance.

2.2.5.2. LCPD in semiconductors. Sub-nanometer resolution LCPD has also been observed on a variety of semiconductor surfaces including: Si [19,20,24,26,37,38], TiO_2 [16,22,39], InSb [23]. Fig. 10 shows simultaneously obtained CPD and topography images of InAs(001)-(4 × 2) surface using FM mode KPFM (note that the experimental results in Fig. 10 were performed by the authors). InAs(001)-(4 × 2) has a row-trough structure consisting of In rows of atoms and pairs of In dimers located in the trough [40]. The trough region has LCPD peaks. The bulked dimers in the trough probably cause the LCPD in the trough. The LCPD peaks indicate a change in the tip–sample interaction.

Okamoto et al. [41] proposed a model to explain the LCPD contrast on a Si(111)-(7 × 7) surface including contrast reversal upon tip conditioning, previously reported by Shiota et al. [38]. Fig. 11 shows atomically-resolved topography and CPD images of a Si(111)-(7 × 7) surface [38]. Fig. 11(b) shows a contrast reversal at the position indicated with X, where the bright spots become dark. Okamoto et al. separated the electrostatic force (F_{ES}) from the topographical force (F_{top}), where the F_{ES} is a function of frequency and F_{top} is a function of frequency and applied bias (V_{DC}) [41]. The measured LCPD is affected by the sum of the two forces. The F_{top} displays cubic-root-like dependence on $V_{applied}$. The resulting sum of the F_{ES} and F_{top} generates multiple intersects with zero force, meaning multiple stable LCPD values. The derived expression for the two new stable points is [41]:

$$V_{DC} = V_{CPD} \pm \frac{\left| f_{top}(\omega, \Delta V) \cos \Delta\theta \right|}{(\partial C/\partial z) V_{AC}}, \tag{2.21}$$

where f_{top} is the modulation component of the topographical force, V_{AC} is applied AC potential, C is the capacitance, and $\Delta\theta$ is the phase difference between the F_{ES} and F_{top} signals. A spectroscopy experiment on the Si(111)-(7 × 7) surface by Arai et al. shows the presence of two separate minimums in the frequency shifts versus sample bias [19], supporting the Okamoto's model of LCPD on semiconductors. The model denotes $f_{top}(\omega)$ as the short-range force responsible for the LCPD contrast. The short-range force is derived from the apex atom's interaction strength with the surface. The difference between semiconductor and ionic materials is the origin of the short-range force, or the bonding force. The characterization of the short-range force as a covalent bonding interaction for semiconductors is consistent with previous experimental studies of Au clusters on Si. The Au clusters shows higher potential than underlying Si substrate, due to a weaker bonding of Au–Si compared to Si–Si interactions [26]. The model is also consistent with the experiments where the LCPD is used for atom identification on a mixed Si–Sb surface [20].

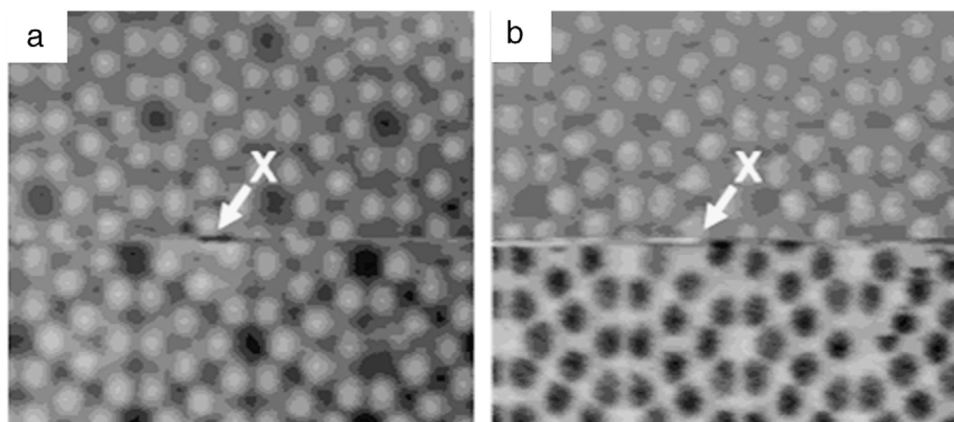

Fig. 11. Atomically-resolved KPFM images of Si(111)-(7 × 7) with contrast reversal. (a) Topography and (b) CPD of Si(111)-(7 × 7) surface. X indicates the location of a spontaneous contrast reversal.
Source: Adapted from [38].

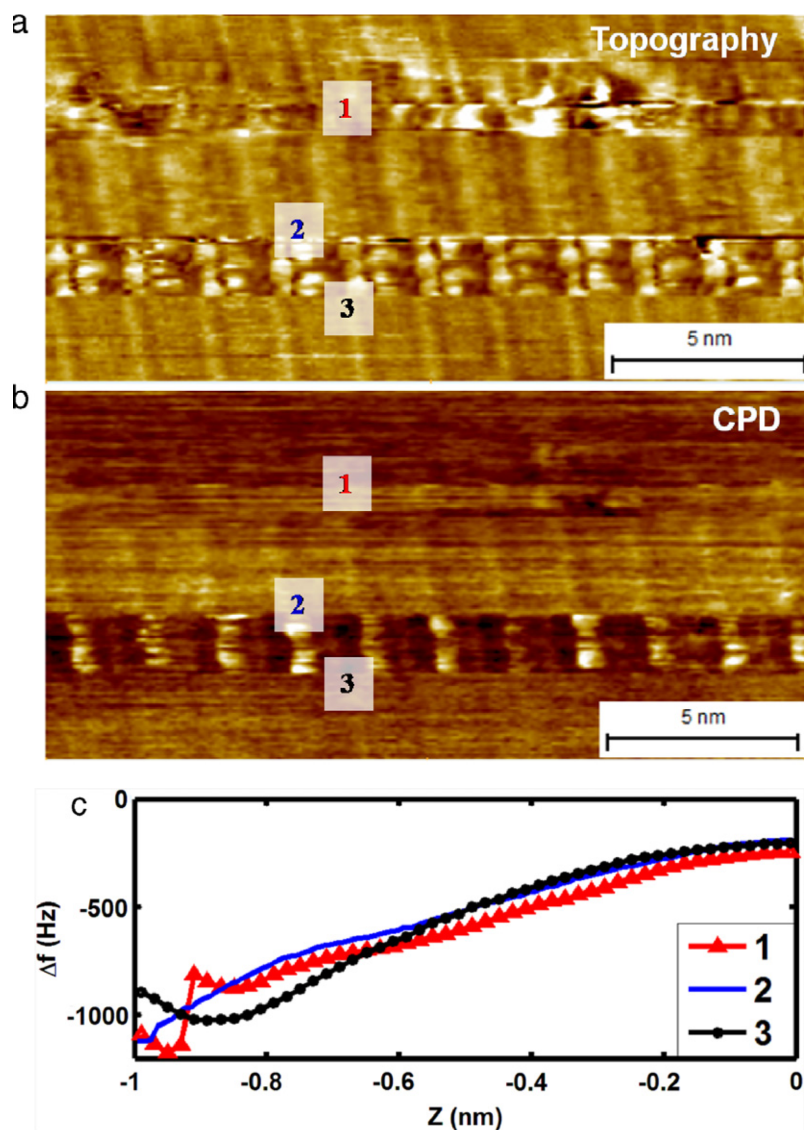

Fig. 12. Tip conditioning for LCPD contrast. (a) Topography and (b) LCPD images of InAs(001)-(4 × 2) surface. The contrast changes at position 1, 2 and 3. At positions 1 and 2, the tip gently touched the surface rearranging the apex of the cantilever, causing the LCPD contrast change. The LCPD contrast spontaneously reverses due to the tip-state change. (c) $df\ (z)$ spectroscopy curves at points 1, 2 and 3 showing force–distance dependence changes induced by different tip state. (Experimental results performed by authors.)

The chemical state of tip and tip–sample distance can affect the measured LCPD on a semiconductor surface. Fig. 12 shows LCPD contrast changes due to the different tip condition caused by gentle tip crashing onto the sample surface. LCPD contrast is not observed initially between the row and trough on InAs(001)-(4×2) surface (note that the experimental results in Fig. 12 were performed by the authors). After gentle crashing of the tip onto the surface (position 1), LCPD contrast can be observed between row and trough. The sudden jump in the frequency shift (df) vs. z spectroscopy curve (curve 1) may imply that the tip crashes into the sample surface. The tip crashing may rearrange the atoms on the apex of tip, which may change the chemical state of tip-end and the tip–sample distance. At position 2, the tip crashes again, and the LCPD contrast increased significantly. However, at position 3, the contrast spontaneously reverses, caused by the alteration of the apex structure by the interaction with the surface. $df(z)$ spectra are taken at points 2 and 3 [curves 2 and 3 in Fig. 12(c)] and showed different force–distance dependence, which imply that the tip states are changed.

In summary, the LCPD contrast is an effect of a bias dependent short-range interaction force between the tip apex atom and the underlying surface. The mechanism of this interaction force will be highly dependent of the system of interest. For a Si tip imaging a semiconductor surface, the short-range interaction is likely to be caused by covalent interactions similar to atomically-resolved non-contact AFM [7]. Similarly, the ionic interactions between the tip and the surface produce the ionic solid short-range force. The measured LCPD is not a true representation of any one electrostatic, covalent, or ionic interaction. The LCPD is a function of the bias dependent short-range forces that apply to the particular sample type. Currently, no sub-nanometer resolution LCPD has been reported for a non-polar surface such as a metal surface. Further studies will make it clear which short-range force dominates the LCPD contrast for particular systems. The LCPD is also a combination of both the microscopic and mesoscopic interactions. The combination of these interactions causes an over-estimation of the true surface potential distribution, making physical interpretations of experimental results of LCPD measurements difficult. Recently, Sadewasser et al. suggested the LCPD variation on a semiconductor surface is caused by the formation of a local surface dipole, due to the charge transfer between different surface atoms or the charge redistribution by the interaction with AFM tip [42]. Models including accurate tip geometries and tip–sample separations are needed for the extraction of physical values from the measured LCPD. Theoretical calculations for both ionic solids and semiconductors show the tip geometry effects on the measured LCPD. Further theoretical analysis is needed to develop modeling tools to extract meaningful results from the measured LCPD. Nevertheless, the LCPD can give insight to the surface electronic properties.

3. Application of high-resolution KPFM

The following section reviews the application of high-resolution KPFM to characterize the electrical properties of metallic nanostructures and semiconductor surfaces and devices. Since the work function or surface potential strongly affect the chemical and physical phenomena taking place at the surface, KPFM reveals critical information on the physical and chemical changes of the surface condition, needed for understanding physical and chemical phenomena on metal/semiconductor surfaces and devices.

3.1. Electrical properties of metallic nanostructures

In recent years, metallic nanostructures have been used in new devices such as high-efficient heterogeneous catalysts [43–45] and high-sensitivity chemical/biological sensors [46]. For these applications, charge transfer between metal nanostructures and substrates (in heterogeneous catalysts), and between metal nanostructures and chemical/biological molecules interfaces (in chemical/biological sensors) are critical to describe and understand. The charge transfer inherently modulates potentials on the metal nanostructure. Therefore, KPFM provides insight into the physics of metal-nanostructure device applications.

3.1.1. KPFM on metallic nanostructures

Gold is a model material to study the formation of metallic nanostructures, due to the stable chemical properties and large atomic size. Goryl et al. showed the work function of deposited Au nanostructures was independent of the size of the Au nanostructure [23,47]. Fig. 13(a) and (b) show the topography and corresponding work function mapping of Au nanostructures grown on InSb(001) surface at 400 K. Au grows predominantly in rectangular island shapes. The typical height of a Au nanostructure is a few monolayers (MLs) (about 2.0 nm).

The work function mapping provides more details about surface topography. The small features, difficult to observe in the topography image due to a large variation in topography, are distinguishable with the help of the work function signal. The small features between Au nanostructures are indicated by arrows in Fig. 13(a) and (b). The work function of small features is the same as the Au nanostructures, which implies the chemical composition of the small features is similar to the Au nanostructure. KPFM is able to give information about the chemical composition of nano-scale features. Graham reported the measured work function on a Au/W(001) system saturates at a coverage of 3 MLs Au, which is close to the work function value of bulk Au [48]. Adsorbate–substrate reactions can also be observed. The contrast between the Au nanostructures and InSb substrate is reversed after high temperature annealing, because a Au nanostructure has lower work function than the substrate after post-deposition annealing (PDA) at 650 K for 2 h. This suggests a Au nanostructure might react with the InSb substrate and form alloys with In atoms, resulting in a decreasing working function of the nanostructure. Note that the surface potential of the InSb substrate did not change after PDA.

Depending on the substrate and surface defects, metallic nanostructures can form different structures. Recent KPFM results show surface potential differences between terrace and step edges on UHV-cleaved semiconductors, alkali halides, and insulating materials, attributed to charged defects [18,49,50]. Charged defects are considered to be nucleation sites for metallic nanostructure growth [51,52]. Barth et al. have investigated Au nanostructures on alkali halide (001) surfaces using KPFM to study whether metal nanostructures will screen defect charges or become charged [53], an important factor for catalytic processes. The charge transfer will significantly affect the surface and nanostructure properties. Finally, charge transfer will change states governing the catalytic reactivity of adsorbates [54].

Fig. 14(a) and (b) show the topography and surface potential images of a UHV-cleaved KCl surface. The bright features on potential image show 0.7 eV larger work function than the rest of the surface terrace sites, attributed to the charged defects. For 0.04 MLs, Fig. 14(c) and (d), and 1.44 MLs, Fig. 14(e) and (f), of Au deposition at 200 °C, Au nanostructures are homogeneously distributed over the terraces with an increased density at step edges, which causes one-dimensional nanostructure growth. KPFM results show that some of Au nanostructures have higher work functions than other Au nanostructures, although they look very similar in topography images. One explanation is the nanostructures with higher work function exist above the charged surface defects. After Au deposition, charge transfer may occur between surface defects and Au nanostructures deposited on the defects. The charge transfer from defects to Au nanostructures increases the work function.

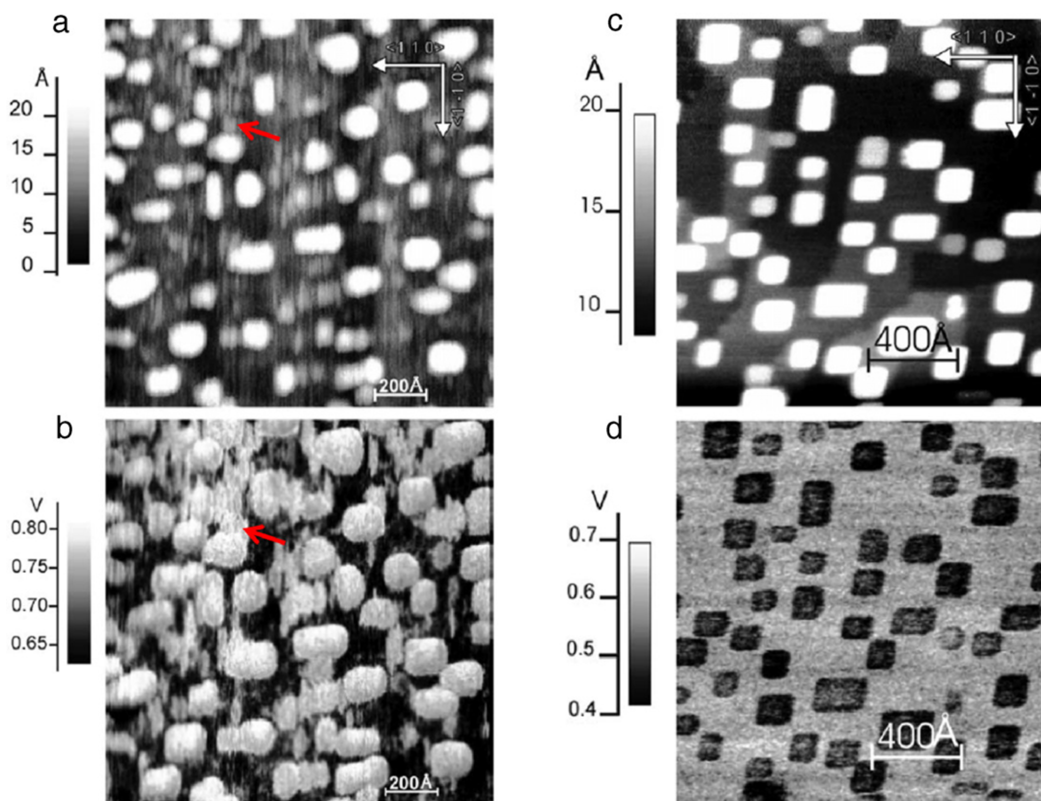

Fig. 13. The topography and work function profiles of Au nanostructures on InSb(001) surface with and without post-deposition annealing (PDA). (a) FM mode KPFM topography and (b) corresponding work function mapping of 0.2 MLs Au grown on InSb(001) surface at 400 K. (c) FM mode KPFM topography and (d) corresponding work function mapping of Au deposited on InSb surface at 300 K with PDA at 650 K for 2 h. The small features between Au nanostructures are highlighted by arrows in Fig. 13(a) and (b).
Source: Adapted from [47].

3.1.2. Charge transfer in metallic nanostructure catalyst

Metallic nanostructures supported on thin oxide films such as TiO_2 or MgO are known to exhibit extraordinary catalytic properties in oxidation reactions [43,51,55–57]. In catalytic reactions, charge transfer between metallic nanostructures and supported oxide films is important to investigate, since the charge transfer from a metal nanostructure to the supporting substrate can affect catalytic reactions on the metal surface. Recently, Gross et al. used a q-Plus non-contact AFM/KPFM system to probe single atoms on the surface [58]. They show KPFM not only allows single atoms to be imaged, but also can be used to detect the charge state of a single atom on thin insulating films.

For the model system, single Au atoms on bilayer ultrathin NaCl films on Cu(111) are used as shown in Fig. 15(a). In constant height imaging mode, frequency shift signals were recorded, Fig. 15(b). Charging of a gold adatom by one electron charge increased the force on the AFM tip by a few pico-newtons, indicating a higher attractive force above a negatively charged Au atom (Au^-) than above a neutral Au atom (Au^0). Density function theory reveals that the large ionic polarizability of the NaCl film is responsible for the stability of the two different charge states [59]. An additional electron on the gold atom forces the Cl^- ion underneath a Au atom to move downward, whereas the surrounding Na^+ ions move upward. This relaxation pattern creates an attractive potential for the additional charge on the Au atom, which is consistent with increase in the absolute value of frequency shift. This work showed a very high sensitivity for detecting the single electron charge. The high sensitivity was achieved by using very small oscillation amplitude (typically 40 pm) and low temperature (5 K) imaging. Note that the experiment was done by a tuning folk system [60], not by a typical cantilever and optical detection scheme.

Fig. 16 shows the frequency shift (Δf) measured as a function of the voltage above Au^- and Au^0 [58]. By determining the peak position (Δf^*) of the parabolic curve obtained in a $\Delta f(V)$ measurement above Au atoms, LCPD is obtained. Switching from a neutral charge state to a negative charge state results in a Δf^* shift of -0.11 ± 0.03 Hz and a LCPD shift of $+27 \pm 8$ mV. The same method was used to investigate Ag atoms with Au atoms on bilayer NaCl on a Cu(111) substrate to show that positive, neutral, and negative charge states can be distinguished and determined with non-contact AFM/KPFM, since both neutral Ag^0 and the positively charged Ag^+ adatoms are stable on bilayer NaCl on a Cu(111) substrate. KPFM techniques illustrate discrimination of positively charged, neutral, and negatively charged atoms based on the LCPD shift measured.

Pt/TiO_2 is another good model system, well-known for applications in photocatalysis water purification and gas-sensing. Under UV light irradiation, the electrons excited in TiO_2 are injected into the Pt nanostructures [61,62], which change the charge distribution on the Pt nanostructures and TiO_2 substrate [39,63]. Fig. 17(a) and (b) show the topography and work function mapping of Pt evaporated on a TiO_2 surface. As shown in the histogram, Fig. 17(c), bright spots shown in Fig. 17(a) are Pt nanostructures with small range of heights (0.12–0.48 nm, mean = 0.30 nm) and diameters (2–4 nm, mean = 3.2 nm). In Fig. 17(b), the brighter areas correspond to larger work functions. The work function on a Pt nanostructure is smaller than on the supporting material, TiO_2. The authors think the electric dipole formation, due to the electron charge transfer from Pt nanostructures to the TiO_2 substrate, causes work function differences between Pt nanostructures and the TiO_2 surface. Fig. 17(e) shows the work function on the Pt

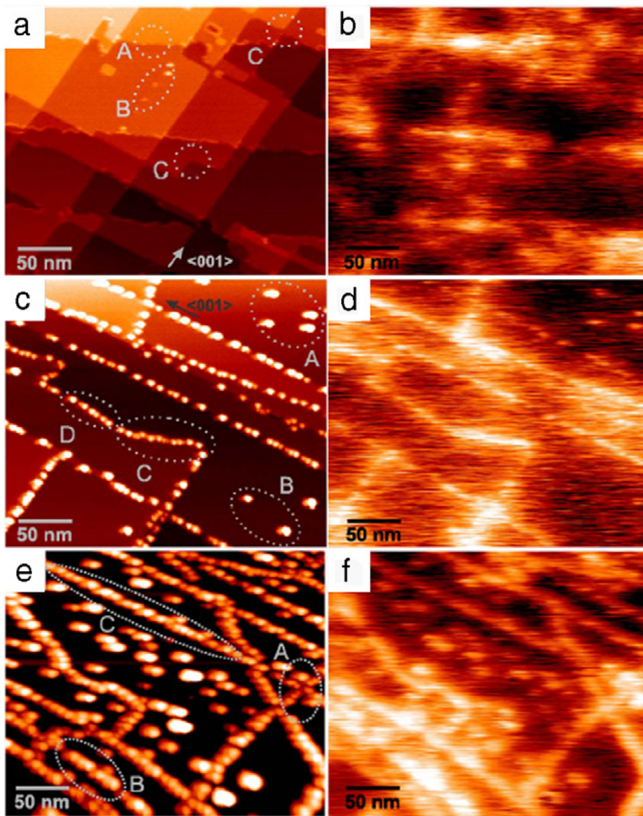

Fig. 14. The topography and work function images of UHV-cleaved KCl, surface with different coverages of Au. Topography, (a), (c), and (e), and simultaneously recorded surface potential images, (b), (d), and (f), of the clean KCl(001) surface, (a) and (b), the same surface after a deposition of 0.04 ML Au at room temperature, (c) and (d), and 1.44 ML of Au at 200 °C, (e) and (f). The clean surface was prepared by UHV cleaving and annealing at 120 °C for 2 h.
Source: Adapted from [53].

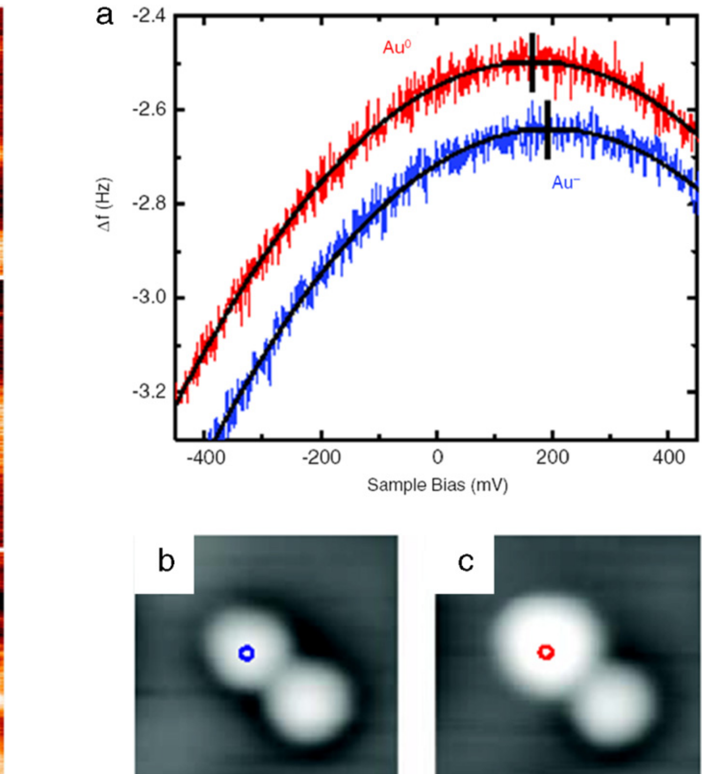

Fig. 16. Examples for charge transfer of Au atoms. (a) The frequency shift (Δf) measured as a function of the voltage above Au^- and Au^0. Both measurements are performed without moving the tip. After measuring $\Delta f(V)$ above Au^-, the charge state is switched to Au^0 by applying a bias pulse of -1 V for a few seconds. Parabolic fits and corresponding parabolic peaks are indicated. Scanning tunneling microscopy images before (b) and after (c) the $\Delta f(V)$ measurements confirm the charge-switching event and show that the switched Au atom has maintained its lateral position.
Source: Adapted from [58].

nanostructures decreases as the interface area between Pt nanostructures and supporting TiO_2 substrate increases. The linear dependence of the work function on the interface area is similar for terrace areas and step edge areas, as shown in Fig. 17(e). Individual Pt adatoms and Na adatoms donate electrons to the

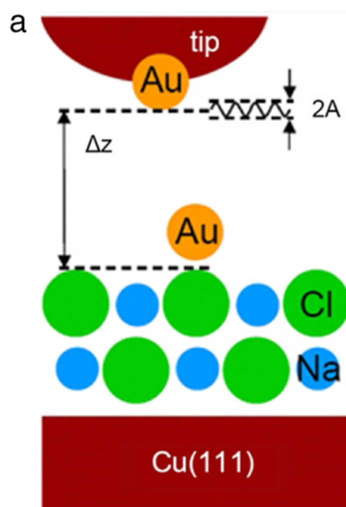

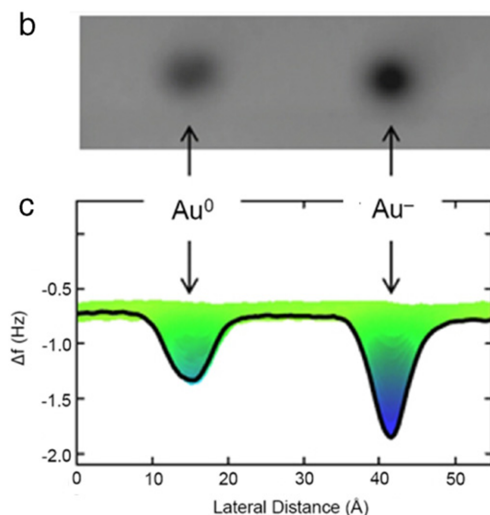

Fig. 15. A schematic diagram of AFM measurement and frequency shifts of Au adsorbed on NaCl/Cu(111). (a) Model geometry of the experimental setup for the AFM measurements of Au/NaCl. Au, Cl^-, and Na^+ are colored gold, green, and light blue, respectively. (b) Frequency shifts recorded in a constant height mode ($\Delta z = 5.0$ Å, $V = -5$ mV, and $A = 0.3$ Å). (c) Line scan of the frequency shift through the center of Au^0 and Au^- atoms shown in (b). The color scale in (c) corresponds to the Δf values, in a three-dimensional representation of the cut along the line profile. (For interpretation of the references to colour in this figure legend, the reader is referred to the web version of this article.)
Source: Adapted from [58].

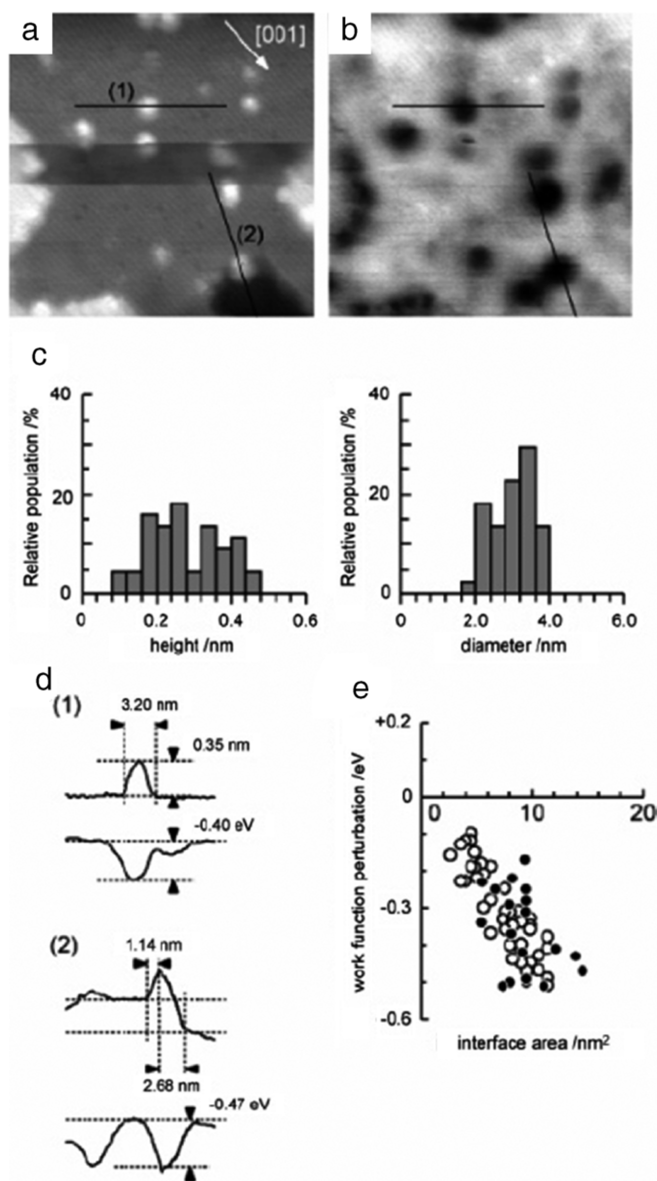

Fig. 17. Examples for charge transfer in Pt nanostructures. (a) Topography and (b) work function mapping of Pt evaporated onto a TiO_2 surface. (c) Distribution of the heights and diameters of the Pt nanostructures formed on the terraces. (d) Cross-sections obtained along the lines in images (a) and (b). (e) Deviation of the work function of the Pt nanostructures on the TiO_2 surface, plotted as a function of the nanostructure/TiO_2 interface area. Open and filled circles are obtained on the Pt nanostructures formed on terraces and steps edges, respectively.
Source: Adapted from [39].

TiO_2substrate [39,63]. Cl adatoms accumulate electrons from the TiO_2 substrate [64].

Recently, Glatzel et al. demonstrated the contacting of single molecular structures assembled on insulating surfaces by a metallic nanostructure, a major step toward functional molecular assemblies, providing possibilities to study molecular conductance [65]. KPFM results showed surface potential differences, with nanometer resolution, between metallic nanostructures, molecules, and the supporting insulating surface, were a function of the local surface potential and the local dipole moment. With further extension, charges can be added or removed at specific sites of the molecules with the metallic terminals. Subsequently, the whole molecule or molecular network can be characterized by KPFM to investigate the charge transport [66].

3.2. Characterization of electrical properties on semiconductor nanostructures

3.2.1. KPFM on semiconductor surfaces

The published reports on atomic-resolution KPFM on semiconductor surfaces is dominated by Si surfaces [19,20,24,26,37,42,67] but also include other surfaces such as TiO_2 [16,22,39], GaAs [68] and InSb [23]. Properties, such as force distribution on a surface reconstruction, surface defects, phase state, and atomic composition, have been investigated using KPFM.

3.2.1.1. Short-range force distribution on a surface reconstruction. Atomic-resolution KPFM can map topography along with the potential dependent forces, providing vital information on the interaction properties of the surface atoms. Enevoldsen et al. observed a 20 meV potential variation between the row and trough of a $TiO_2(110)$ surface, as seen in Fig. 18 [16]. AM mode KPFM with a 70 kHz Pt/Ir coated cantilever was used to achieve atomic resolution. The row spacing on the TiO_2 (110) was measured as $\sim$1 nm. The LCPD profile shows a two-peak pattern. The large peak indicates the attractive force to the five-fold coordinated Ti [Ti(5c)] surface atoms. The dark feature is the repulsive force with the two-fold coordinated O [O(2c)] row atoms. KPFM was employed to resolve the row/trough structures on InSb [23] and InAs. The short-range force on semiconductor surfaces is smaller than on ionic solids, so the LCPD signal will be smaller. Krok et al. studied InSb(001) surfaces and observed a 5 meV dip on the In rows [23]. To obtain the row-trough resolution for InSb(001), a 111 kHz Si cantilever is used in FM mode. InSb has a row-trough structure (row distance $\sim$1.7 nm) and a dip in the LCPD at the In row.

3.2.1.2. Surface defects. One of the most interesting and potentially useful applications of the atomic-resolution KPFM is the visualization of single defects or step edges on the surface. Using atomic-resolution KPFM, single vacancy defects can be imaged directly. KPFM can provide an insight into the electronic properties of defects on the semiconductor surface. Shiota et al. observed a vacancy defect on Si(111)-(7 $\times$ 7) with atomically-resolved KPFM images, shown in Fig. 19 [38]. The potential energy of the corner hole (arrow in Fig. 19) is 61$\pm$9 meV higher than the corner adatom and 77 $\pm$ 5 meV higher than the center adatom. The vacancy has dangling bonds, which increases the short-range interaction with the tip, causing an increase in the LCPD.

KPFM can be used to study defects larger than vacancies, such as step edges or grain boundaries. Glatzel et al. has observed a 15 meV decrease and a 40 meV increase of the surface work function for cleaved p-type and n-type GaAs(110) steps, respectively as seen in Fig. 20 [50]. Glatzel et al. also measured a 130 meV decrease and a 40 meV increase of the surface work functions on cleaved p-type and n-type GaP(110) steps, respectively [50].

KPFM can investigate the effects of surface band structure on the charge state of semiconductor surfaces. For III–V semiconductors, the (110) orientation is a common surface for cleaved samples. The (110) surface of III–V semiconductors normally exhibits flat band conditions. The surface work functions should be similar to bulk values [69]. However, step edge traps or defects can introduce mid-gap surface states, which influence the surface Fermi energy level. The change in the CPD reflects the direction and amount of band bending caused by these surface states. The decrease of the measured work function for p-type materials is consistent with bands bending down, positioning the surface Fermi level in the band gap. For midgap states in n-type materials, the bands bend up to position the Fermi level in the band gap, thereby increasing the surface work function. KPFM is well suited to study the effects of surface defects on electronic properties with high spatial resolution. KPFM studies on surface electronic states have application in the development of devices with large surface property effects, such as laser diodes or solar cells.

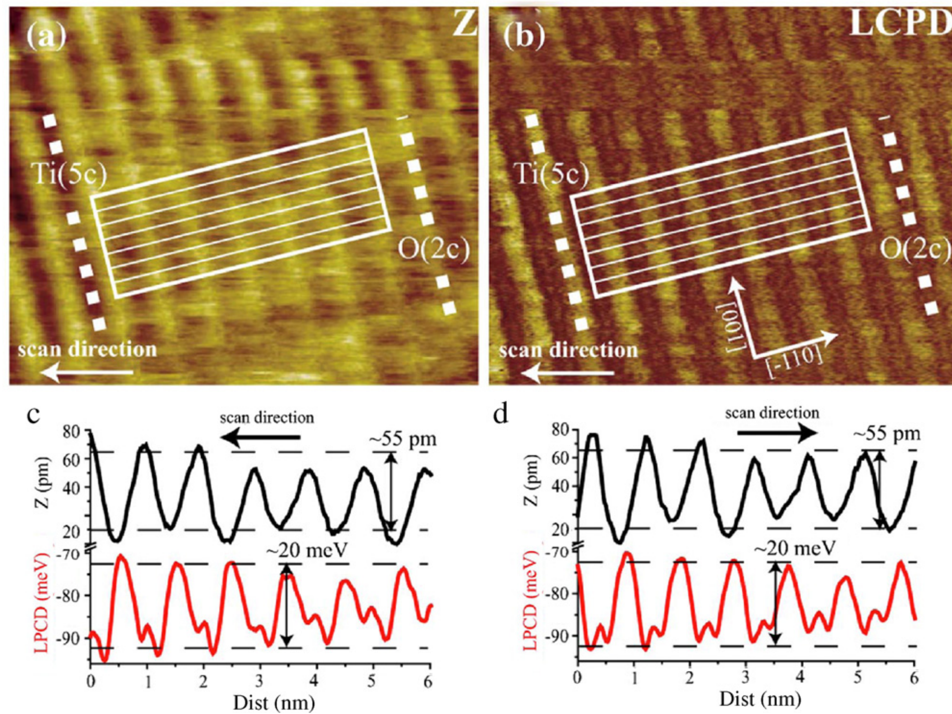

Fig. 18. Atomic-resolution KPFM image of TiO_2 (110) surface. (a) Topography (Z) and (b) LCPD of TiO_2 (110), image size 10×8 nm^2. (c) Line scan average of topography and LCPD indicated on image as rectangle box.
Source: Adapted from [16].

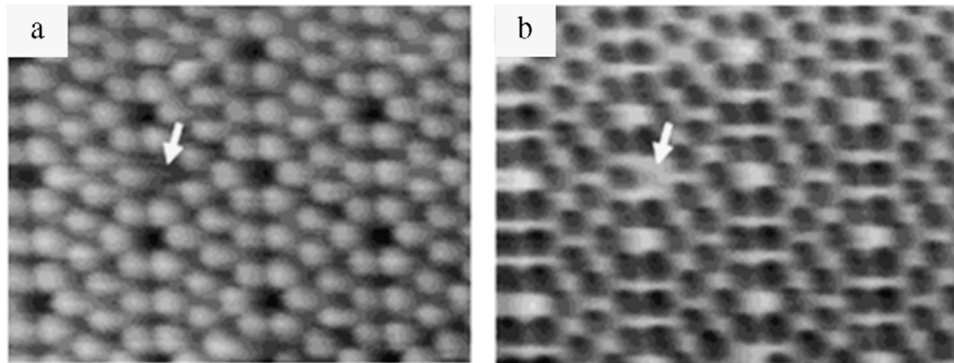

Fig. 19. Atomic-resolution KPFM images of Si(111)-(7 × 7) with vacancy. (a) Topography (b) LCPD images of the Si(111)-(7 × 7) surface with 7×10 nm^2 scan size.
Source: Adapted from [38].

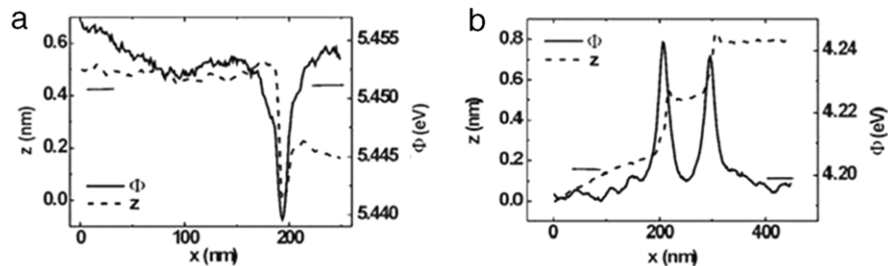

Fig. 20. Line profiles of topography (dashed line) and work function (solid line) measured by KPFM through a atomic step on (a) p-type and (b) n-type GaAs(110) surface, respectively. A 15 meV decrease and a 40 meV increase of the surface work function are observed for cleaved p-type and n-type GaAs(110) steps.
Source: Adapted from [50].

3.2.1.3. Reconstruction identification. The high-resolution KPFM has been used for identification and comparison of different surface reconstructions on a semiconductor surface. A 0.5 eV potential difference is measured between mixed Au/Si(111)-(7 × 7) and (5 × 2) surface reconstructions [24]. Fig. 21(a) and (b) shows the 500 × 500 nm^2 CPD and topography of Au/Si(111) mixed (7 × 7) and (5 × 2) surfaces. Initially, the reconstruction phases are identified, as seen in Fig. 21(e) and (f), using scanning tunneling microscopy (STM). The position of the Fermi energy level at the surface is dependent on the surface electronic states. Different surface reconstructions induce different surface electronic states, resulting in different Fermi energy levels on the surface.

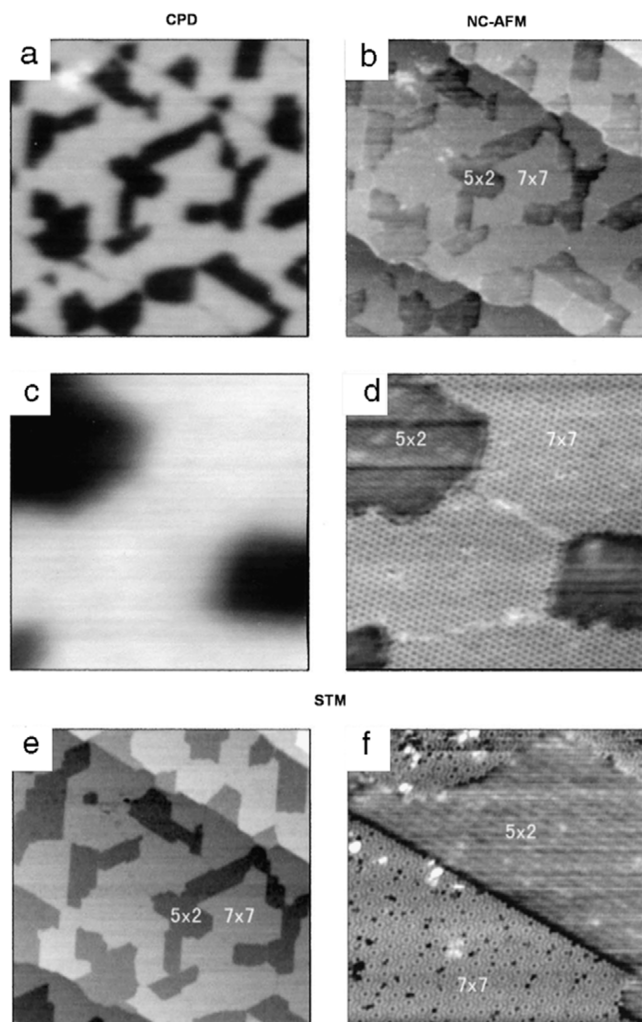

Fig. 21. KPFM and STM images of a mixed Si surface with (7×7) and (5×2) reconstructions. 500×500 nm^2 (a) CPD (b) topography images of the Au/Si(111) mixed (7×7) and (5×2) surface. 100×100 nm^2 (c) CPD (d) topography images on the same surface. The (7×7) reconstruction has a 0.5 eV higher CPD than the (5×2) reconstruction. (e) 500×500 nm^2 (f) 50×50 nm^2 STM images on the same surface showing clear surface reconstruction.
Source: Adapted from [24].

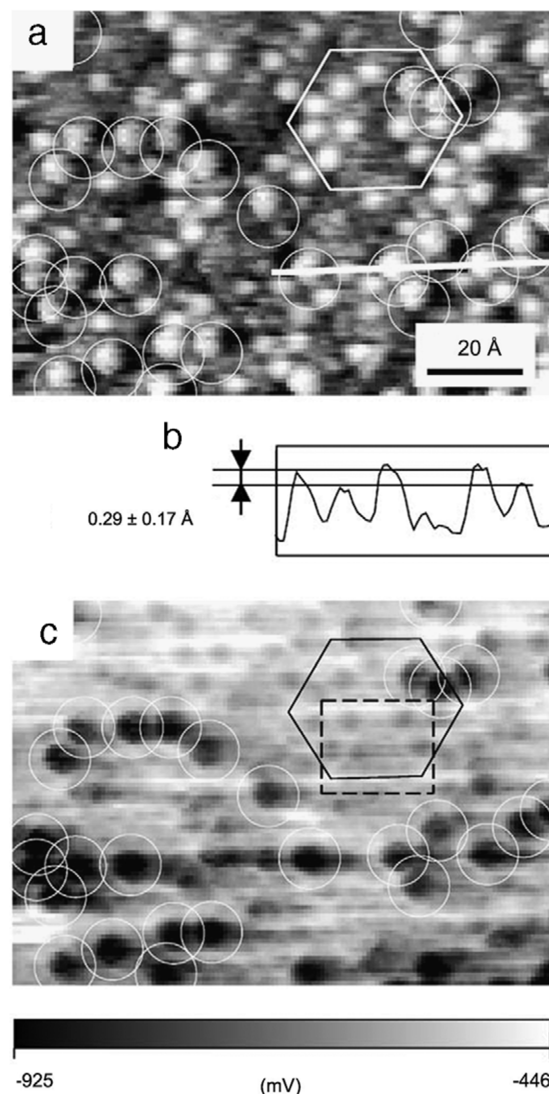

Fig. 22. KPFM images of mixed Sb–Si surface. (a) 121×85 Å^2 topography image of the Sb induced Si(111)-$\left(5\sqrt{3} \times 5\sqrt{3}\right)$ surface reconstruction. Circles indicate the Si adatoms which are 0.29 ± 0.17 Å higher than the Sb adatoms. The hexagon indicates the unit cell. (b) Topography line scan illustrating the height difference between the two types of adatoms. (c) CPD image of the sample location on the Sb induced Si(111)-$\left(5\sqrt{3} \times 5\sqrt{3}\right)$.
Source: Adapted from [20].

Surface dipoles can also introduce a change in the measured CPD. Similar work has been reported on clean Si(111), showing a 0.11 eV difference between the (7×7) and (1×1) mixed surface reconstructions [67]. KPFM, in combination with other surface analysis techniques, can help separate the different electrical effects of the surface reconstruction on the measured CPD.

3.2.1.4. Atom identification. Okamoto et al. prepared a mixed Si–Sb surface reconstruction and distinguished different surface atoms based on their various tip interaction strengths [20]. This work is the first experimental result using KPFM for atom identification. The combination of topography and CPD image provides a clear distinction between different atoms, difficult to extract from topography imaging alone. For example, Sb is deposited on Si(111) and annealed to achieve the Sb induced Si(111)-$(5\sqrt{3} \times 5\sqrt{3})$ surface reconstruction, (Fig. 22). In Fig. 22(a), the topography image shows two types of bright spots on the surface. The two bright spots show a slight height difference of 0.29 ± 0.17 Å. The Si adatoms (circled adatoms) are the bright spots in the topography. A CPD image of the same surface clearly distinguishes between the two types of adatoms as seen in Fig. 22(c). The circled adatoms, corresponding to lower CPD, are Si, while the other adatoms are Sb. The potential difference between the Si and Sb adatoms is 0.2 eV. The measured difference between Si and Sb disagrees with theoretical work: The Sb state should be 0.6 eV below the Si adatom. This discrepancy sparked the discussion of the influence of the short-range forces involved in atomic-resolution KPFM.

3.2.2. Adsorbates on semiconductor surfaces

One of the simplest applications of high-resolution KPFM is the observation of the interaction properties of an adsorbate on a surface. The potential change provides information about the tip–adsorbate interactions relative to the tip–surface interactions, indicating electron exchange or dangling bonds. An average CPD value is also measured, representing the true surface potential.

Kitamura et al. deposited Au on Si(111)-(7×7), and the Au adsorbates showed a higher potential (lower work function) than the clean Si(111)-(7×7) surface [26]. The potential change corresponds to the change in tip–sample interaction of the Si and Au surface atoms. The Si adatoms on the surface have dangling

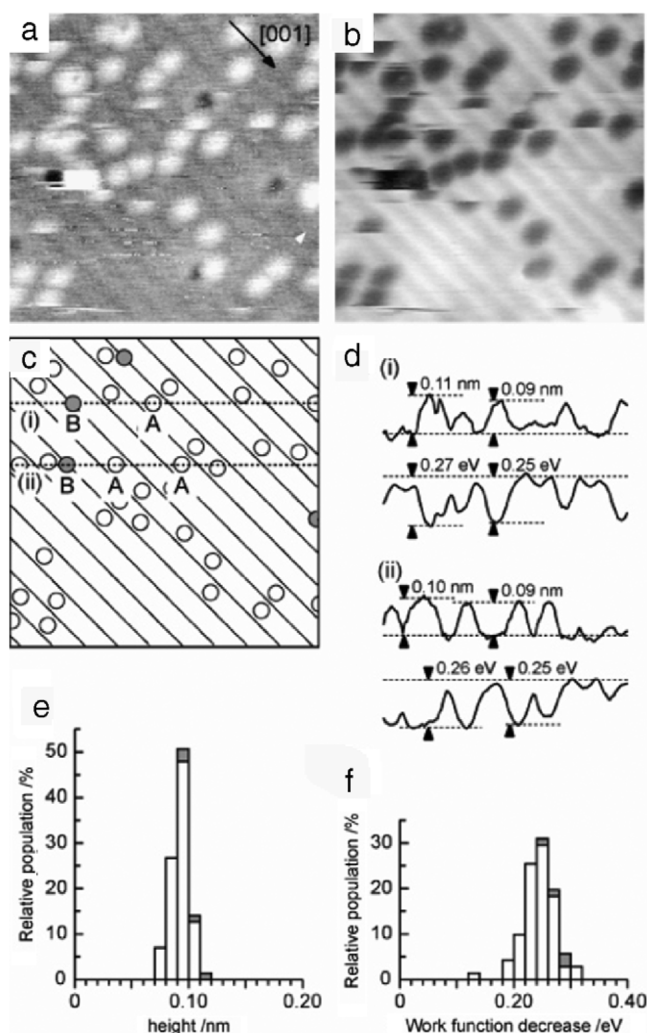

Fig. 23. KPFM images of Pt on TiO_2. (a) Topography and (b) work function mapping of Pt on TiO_2. Image size 10×10 nm^2 (c) Cartoon mapping of the surface indicating the two different bonding sites (white circles site A and dark circles sites B). (d) Line profiles indicating the potential and height differences of the two sites. (e) Height and (f) work function decrease histograms of (a) and (b), respectively.
Source: Adapted from [39].

bonds interacting with the apex of the tip. The metal clusters have delocalized electrons, reducing the tip interaction strength, which reduces the work function.

Ag was also deposited on Si(111)-(7 × 7), and a potential dependence on the size of the Ag aggregates was observed [24]. The Ag "clusters" (aggregates smaller than a few nanometer) show a work function 10 meV smaller than the clean Si surface. When Ag "islands" are formed (aggregates larger than a few nanometers), the work function is approximately 10 meV higher than the measured clean surface. The islands are small crystallites with (111) plane orientation on the Si substrate, whereas the clusters are polycrystalline Ag, which do not have an ordered surface. The work function difference is caused by the difference in electronic properties of the surfaces.

The high-resolution work function mapping can be used to distinguish differences in structures of adsorbates on the surfaces. Pt on TiO_2(110) shows a work function decrease between 0.24 and 0.28 eV [39]. Fig. 23 shows the work function mapping of the Pt adatoms on the clean surface TiO_2(110) surface. The streaks were reported as thermal diffusion of the adatoms on the surface. Two different bonding sites were identified and characterized. Site A is the Pt on the Ti row atom and site B is Pt on O vacancies. The work

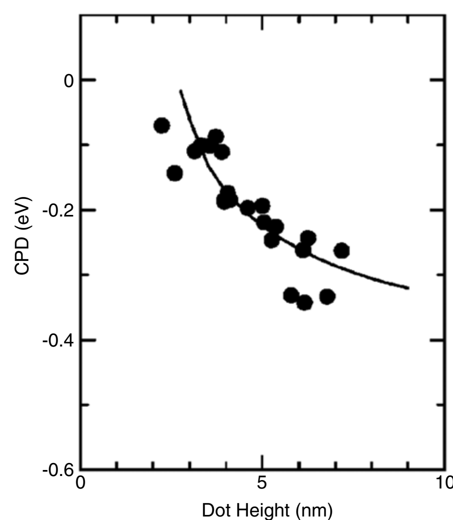

Fig. 24. The height dependence of the CPD of InAs QDs. Filled circles represent collected data of the measured CPD of different InAs QDs on GaAs(001) surface. The solid line shows calculated values using a quantum disk model.
Source: Adapted from [76].

function difference between the two sites is 0.02 eV, consistent with simple bonding models. For site B, more electron transfer causes a lower work function.

3.3. Nano-scale electrical properties characterization in devices

KPFM has demonstrated a unique usefulness in characterizing the properties of various electronic devices, because KPFM can correlate potential distribution with device structures. The versatility of KPFM is featured in studies of many devices; quantum dots (QDs), electrical junctions, transistors, and solar cells. KPFM is compatible with operational devices [70–74], allowing imaging under different performance conditions. High energy resolution KPFM can characterize the single electron trapping in a QD [75].

The influence of surface states changes with device types and material types. Experiments are performed most commonly in air, which can introduce surface states. For absolute work function measurements, surface states will drastically change the measured values. Air may also introduce other variables when the system contains different materials. For example, the native oxide will form with any exposure to air in a system containing InAlAs, whereas GaAs is less reactive to air and might only generate surface states.

Surface states in junctions of a single material can cause a reduction in the measured CPD difference because of band bending in each layer. For example, a p–n junction will show a lower than expected built-in potential. However, after applying an external bias, the full potential change is observable, with little influence from the surface states. External biasing alters the relative references within the device, creating a shift in the measured CPD from the equilibrium state. Surface states will influence measured values, but the changes from equilibrium to excited will be insignificant.

3.3.1. Quantum dots

QDs are used in the development of static memory, lasers, solar cells and many other applications. Studying QDs with KPFM has a significant advantage over STM and photon based methods, because KPFM provides the structure and the potential of the QDs simultaneously. Yamauchi et al. observed a potential dependence on the height of InAs QDs grown on GaAs(001), shown in Fig. 24 [76]. The calculated CPD dependence on the QD size using a quantum disk model (shown as the solid line in Fig. 23) is consistent with experimental results. QDs ranging from 1.3 to

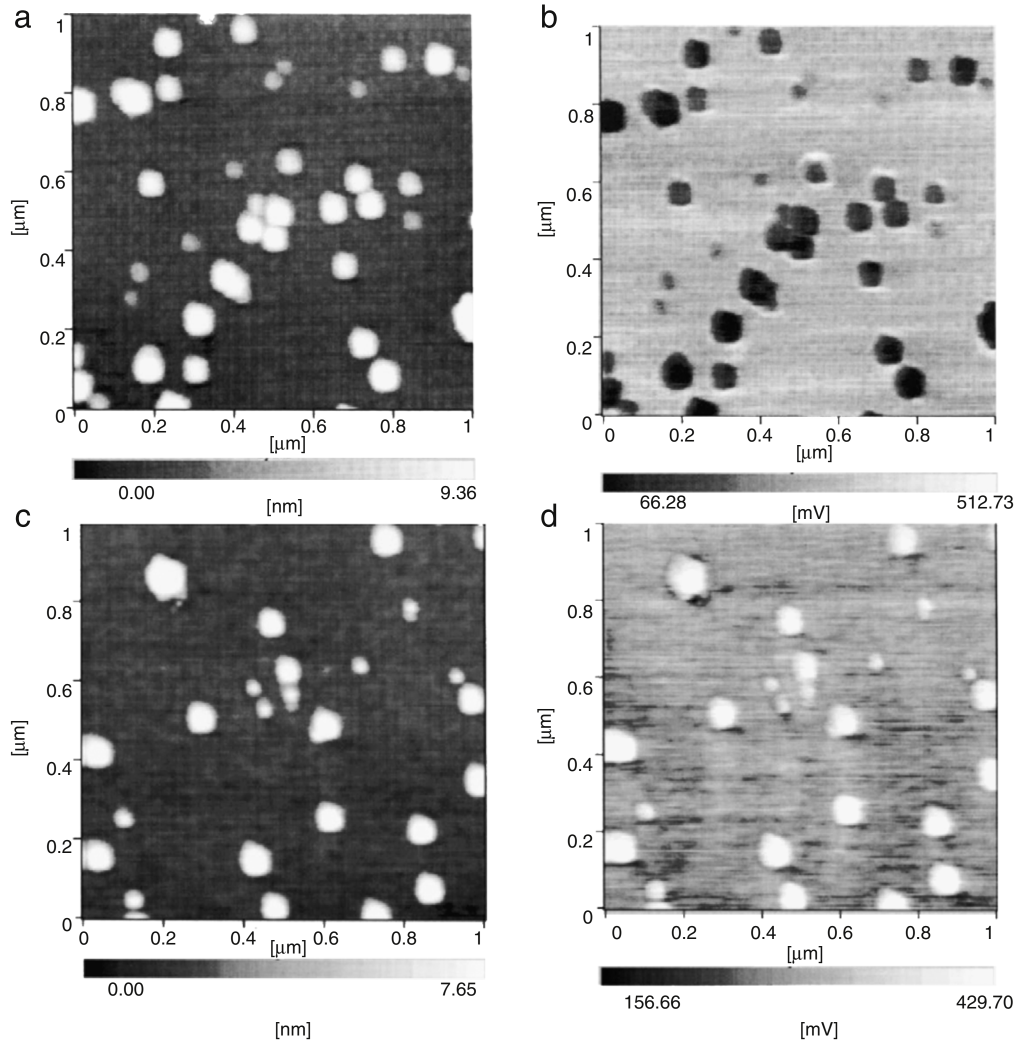

Fig. 25. Charging of Si QDs with KPFM. (a) Topography and (b) CPD images of Si QDs prior to charging. (c) topography and (d) CPD of Si QD after charging by biasing tip with −5 V.
Source: Adapted from [75].

7.2 nm of height and 21.8 to 44.6 nm of width were observed. The height increases with decreasing CPD (filled circles in Fig. 23). The measured CPD includes the potential increase from the quantum size effect. KPFM can explore the properties of the QD itself, while revealing the QDs interactions with the sample surface.

Shusterman et al. investigated InSb QDs and their strain effects on a GaAs surface [77]. Dark rings in the CPD appeared around the InSb QDs. High-resolution TEM confirms the surrounding substrate is strained. The potential change due to the straining of the GaAs lattice, is observable because of the high spatial resolution of KPFM.

KPFM is used to investigate the detailed electrical properties of QDs, particularly their charge states. Salem et al. observed the potential change caused by the charging of Si QDs [75]. Si QDs 2–8 nm in diameter were deposited on SiO_2. Fig. 25(a) and (b) shows the topography and CPD of the uncharged QDs. Placing the tip in contact with the QDs and applying a −5 V bias, for 30 s, charged the QDs. Fig. 25(c) and (d) shows the topography and CPD change after charging of the QDs. The charged QDs shows an increased CPD, while the substrate maintains the sample potential around 300 mV. The estimated potential change due to charging of the QD is [75]:

$$\Delta V = \frac{(ne)^2}{q4\pi \varepsilon d}, \tag{3.1}$$

where d is the QD diameter, n is the number of injected electrons, and ε is the dielectric constant of silicon. Eq. (3.1) is based on the expression for the conduction band energy of a QD after charging. The QD's diameter controls the amount of charge stored in the QD. The CPD is consistent with the capturing of a single electron for QDs with diameter less than 2.8 nm. QDs with 4.7–7.4 nm in diameter have a CPD consistent with trapping of three electrons. QDs with diameters 2.8–4.7 nm are expected to trap two electrons; however, no QDs in that diameter range were observed. The results illustrate how KPFM can be used to investigate electron charging of QDs over various diameters. KPFM shows the added ability to purposely alter electronic properties by providing a nano-scale electrode. Electrons can be injected through QDs via the probe tip during KPFM measurement.

3.3.2. *Junctions and heterostructures*

Prior to the invention of KPFM, KP had been used to characterize electrical properties of junction devices [78–81]. In the last decade, KPFM has become the preferred tool to study 2D potential profiles in semiconductor junctions. Recently, KPFM has been recognized as an exceptional tool to characterize p–n junctions [11,82–88], p–i–n [89,90] and heterostructures [91–94], due to KPFM's high spatial resolution in measuring the surface potential. The impact of surface properties increases as the devices scale down, due

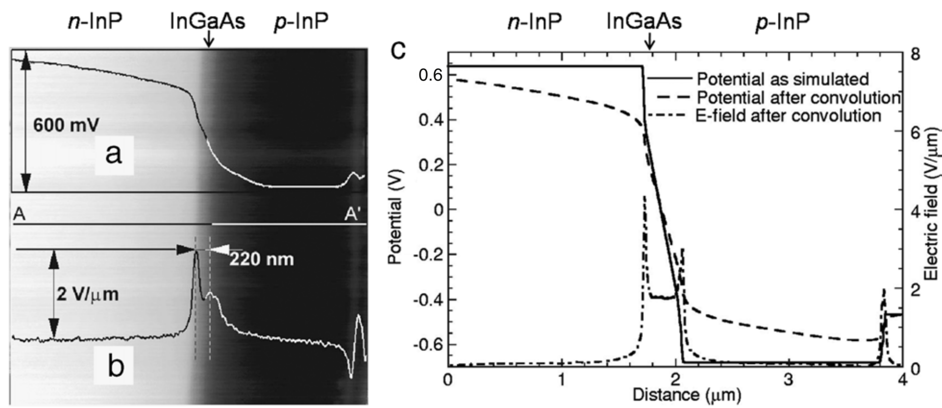

Fig. 26. KPFM on a laser diode. (a) Measured CPD of InP/InGaAsP/InP p–i–n junction showing a 0.6 eV change between n-InP and p-InP and (b) electric field. (c) Calculated potential and electric field profiles using ATLAS/BLAZE from SILVACO, Santa Clara, CA. The electric field is the first derivative of the potential profile.
Source: Adapted from [89].

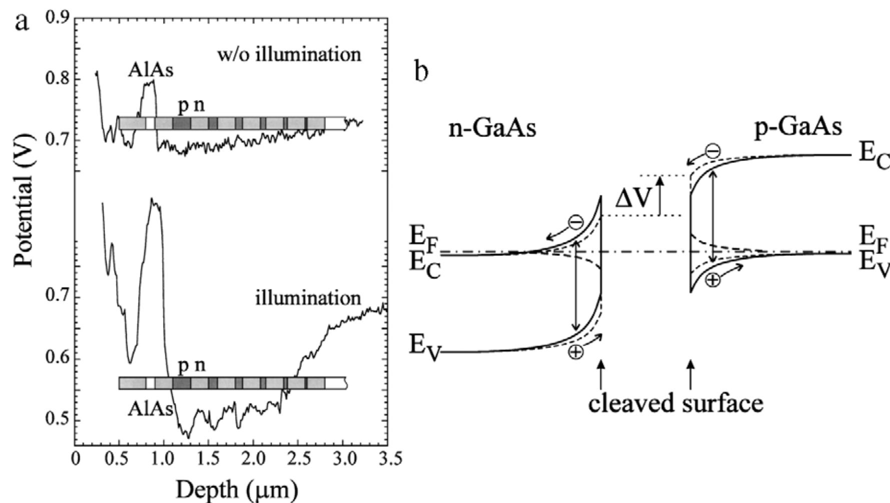

Fig. 27. CPD of multi-junction GaAs samples. (a) Series of GaAs p–n junctions with and without external illumination. With illumination, a contrast is observed between the different layers, and the baseline CPD is reduced to 0.5 eV from 0.7 eV. The baseline CPD is the background CPD level in the junctions. (b) Band diagrams illustrating the charge separation of excited electron–hole pairs from the built-in electric field of the surface. Solid lines indicate the bands without illumination. The dashed lines indicate the bands under illumination.
Source: Adapted from [82].

to surface-to-volume ratio increases. KPFM can be used to measure accurately the surface band bending of scaled diodes and heterostructures. KPFM is a passive technique, allowing the tip to probe the surface without interfering with electronic properties. Compatibility with illumination or external applied biases also makes KPFM an attractive microscopy for junctions.

KPFM measurements are performed mostly on devices in air or on devices exposed to air prior to scanning. Air exposure introduces an interesting complexity to the interpretation of the KPFM results, because adsorbates may introduce or passivate surface states, causing surface band bending. KPFM is extremely surface sensitive. Measured CPD in the presence of surface band bending does not truly represent the bulk potential profiles [32]. In most bulk measurements of device structures, cleaving in UHV avoids modification to the surface potentials from adsorbates or oxide layers.

Robin et al. performed KPFM (in air) on a InP–InGaAsP p–i–n laser diode [89]. Fig. 26(a) shows the measured CPD of the p–i–n diode with 600 meV difference between *p* and n-type InP. The expected potential difference is 1.3 eV. The calculated potential and electric field profiles, shown in Fig. 26(b), are in good agreement with the measured results, with the exception of the magnitudes of the CPD. Surface states caused band bending, which suppressed the magnitude of the CPD change.

KPFM is compatible with external illumination, which can help probe the electronic states on the surface. Diodes are extremely sensitive to excitation, and light may cause changes in the measured CPD. Mizutani et al. observed that a multiple p–n GaAs device under illumination has a baseline potential (the background level of the CPD in the device region) of 0.5 eV compared to 0.7 eV in dark conditions. An increase in contrast between device layers is also seen in Fig. 27(a) [82]. Without illumination, the cleaved GaAs surface shows little CPD difference between n-type and p-type, because of surface states. All the measurements were performed in air and the native oxide was expected to introduce surface states. When illuminated, the electron–hole pairs were separated by the electric field caused by the surface band bending. Holes will accumulate at the surface for n-type and electrons for p-type, as seen in Fig. 27(b). These accumulation layers will cause an increase in the CPD contrast between the n-type and p-type layers.

Loppacher et al. also observed a contrast increase between n-type and p-type Si under illumination [86]. The measured CPD difference between n-type and p-type Si is 320 and 120 meV for illuminated and dark conditions, respectively. The expected difference is 0.8 eV, but the measured difference is only 0.2 eV. This anomaly may imply that surface electronic states dominate the measured CPD and that the illumination has insufficient intensity

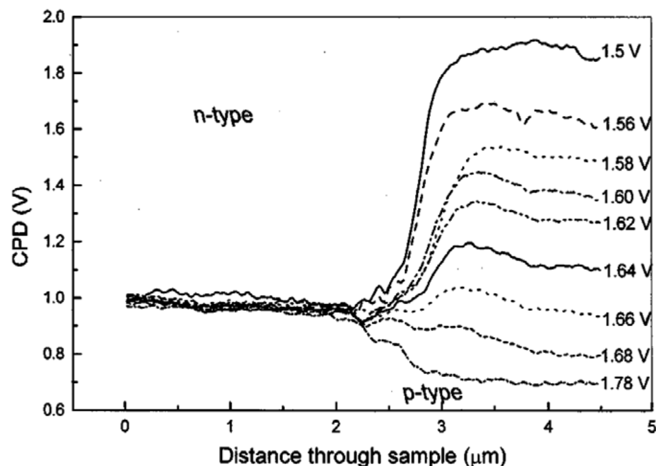

Fig. 28. CPD measurement on an operational GaP LED. Potential profiles of GaP n–p junction under forward biases, from 1.5 to 1.78 V. The built-in potential of an air cleaved GaP diode is expected to be 2 V, but only 1.2 V is measured by KPFM. *Source:* Adapted from [84].

to saturate the surface states. External illumination on a p–n junction increases the CPD contrast, because of the electrons or holes accumulating at the surface.

Conversely, for quantum well structures, external illumination causes a drop in the measured CPD because of charge screening. Chavez-Pirson et al. observed a screening effect for an illuminated n–i–p–i AlGaAs quantum structure [91]. Illuminating the structure increases the baseline CPD about 70 meV and reduces the potential contrast. A difference in band bending of n-type and p-type under illumination causes the baseline increase. The contrast between n-type and p-type layers in CPD is reduced, because a screening of the electric fields at the junction occurs from the excited electron–hole pairs. External illumination can help to suppress surface states. However, illumination is not ideal for every system, because the devices' structure can have a larger dependence on the photo-generated electron hole pairs than on the surface state.

The diffusion lengths of the photo-generated carriers have been measured on a p–n junction by high-resolution KPFM. For GaP p–n junctions, Meoded et al. measured hole diffusion lengths and their dependence upon illumination intensity [87]. The intensity of the illumination source was varied. The CPD profile is fitted to the minority carrier continuity equation to determine the expected diffusion lengths. The diffusion length increases with increasing intensity and agrees with the theoretical diffusion lengths.

An external bias can be applied during KPFM measurements, which provides data on junction properties in different modes of operation. Shikler et al. measured the potential profile of an operational light emitting diode (LED) under different applied biases [11,84]. The built-in potential of an air-cleaved GaP diode is expected to be 2 V, but only 1.2 V is measured by KPFM. The decrease in built-in potential can also be explained by surface states from native oxide formation. The surface states act as traps for the majority carriers, which causes a depletion region, bending the bands up and down for n-type and p-type, respectively. Fig. 28 shows the potential distribution of the GaP diode over a range of applied biases. The key feature is the range of applied biases is 0.28 V, while the range of measured CPD in the p-type region is 1.2 V. The increase in built-in potential is photo-voltage induced from recombination of internal emission photons. When applying an external illumination to the diode under different biases, the surface photo-voltage increases with intensity of the external source.

Quantum wells or heterostructures for applications in lasers diodes and photodetectors can be investigated using KPFM. For laser diodes, the measurement of potential changes during operation is extremely useful for determining causes of decreased performance. Ideally, the entire voltage drop should span the active region of the laser diode. Lévêque et al. observed only 30% of the applied bias drops across the active region of an air exposed GaSb laser [94]. The reduction in the potential drop across the active region contributed to a significant voltage drop across the substrate at positive biases and a non-negligible voltage drop across the substrate–cladding interface. For negative biases, a lower voltage drop was measured across the substrate, with a significant voltage drop across the cladding layer. Determining the sources of voltage losses assists designers to improve the performance of laser diodes.

High-resolution KPFM can be applied even to nano-scale heterostructure features to observe variations in CPD. Schwarzman et al. measured the CPD of a GaAsP/InGaAs multi-quantum well solar cells cleaved *in situ* [93]. The 8 nm quantum wells show a barrier height of 10 meV with 45 nm barrier widths. Charging of surface states causes a reduction of CPD difference of n and p+ regions from 1.4 to 0.5 eV.

KPFM also has been used to investigate the mechanisms of critical failure or burnout of a laser diode during operation. Ankudinov et al. investigated a InGaAs/AlGaAs/GaAs heterostructure laser diode cleaved in air with KPFM under different applied biases [90]. Surface charge screening, causing a reduction in the measured voltage drop, occurs in equilibrium to 200 meV from the expected voltage drop of 1.5 eV. The CPD of the laser diode from 0 to 1.7 eV forward biases is shown in Fig. 29(c). At the higher biases, a bump can be seen (indicated by arrow) in the surface voltage drop [Fig. 28(d)]. This bump is a potential drop across the buffer–emitter interface. Parasitic power sinks can cause failure of laser diodes. When the laser diode is biased with high injection currents, the buffer–emitter interface heats and appears to melt, destroying the laser diode. The advantage of KPFM for studying failure mechanisms is the measurement of the device during operation.

KPFM has been shown to be a powerful technique for studying semiconductor heterostructures. Heterostructures can also be used for calibrating the spatial and energy resolution of KPFM. The spatial resolution can be measured directly in the CPD image by having a series of quantum wells with varying thicknesses [92,95]. Usunami et al. performed KPFM on cleaved GaAs/AlAs and InAlAs/InGaAs heterostructures, in air, and were able to resolve a 20 nm layer [95]. Fig. 30 shows the measured topography and CPD of InAlAs layers ranging from 20 to 200 nm thicknesses sandwiched between 200 nm layers of InGaAs.

The challenge for investigating junctions or heterostructures is overcoming surface state effects. Since nearly all measurements are performed in air, which induces native oxide formation. KPFM is an attractive measurement technique for junctions and heterostructures because of the plethora of experiments compatible with KPFM. KPFM has the significant advantage of high spatial resolution for operational devices, yet does not always accurately represent the bulk potential values. The key to accounting for surface states is to integrate the KPFM with other techniques to provide bulk properties. KPFM has great value for measuring the electronic structures of junctions and heterostructures, including band alignment, failure mechanisms, and surface electronic changes from absorption of photons.

3.3.3. *Transistors*

Experimental techniques providing valuable electrical, mechanical and processing properties are critical to the development of FETs (field effect transistors). KPFM provides a two-dimensional profile of surface potentials, ideal for transistor structures. KPFM identifies features causing a decrease of device performance, such as high contact resistances from Schottkey barriers [70].

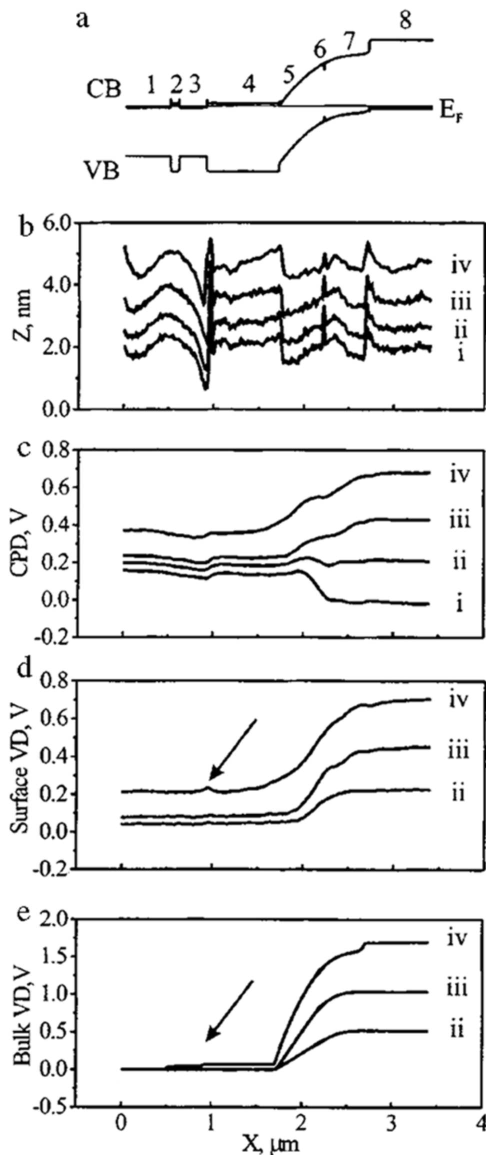

Fig. 29. CPD measurements on a laser diode under applied biases. (a) The band diagram for laser diode. layer 5 and 7 are the cladding and layer 6 is the active region. Other layers are described in detail in the reference. Line profiles of measured (b) topography and (c) CPD for the following biases: (i) 0 eV, (ii) 0.513 eV, (iii) 1.05 eV, and (iv) 1.733 eV. (d) The surface voltage drop is the equilibrium CPD curve subtracted from the CPD profile at a certain bias. The arrow indicates the position of the parasitic voltage drop responsible for the device failure. (e) Calculated potential profile in the bulk.
Source: Adapted from [90].

With cleaved samples, KPFM provides two-dimensional profiles of device characteristics with relations to doping profiles [81,88], operational devices [70,72–74,96] and gate stacks [97].

One of the first measurements of the potential profiles of operating GaAs high electron mobility transistors (HEMTs) was done by Mizutani et al. [73]. These studies of the GaAs HEMTs [73,74,96] and metal semiconductor field effect transistors (MESFETs) [72] employed samples cleaved in air. Air cleavage alters the surface properties by perturbing the surface potential profiles relative to the bulk potential profiles. The surface states cause a shift in the potential profile of about 0.8 eV on GaAs and related materials, but stay relatively uniform, as long as the doping density and semiconductor composition are constant (i.e. Al-containing semiconductors will oxidize differently than Al-free semiconductors) [74]. The oxidation-induced surface states have

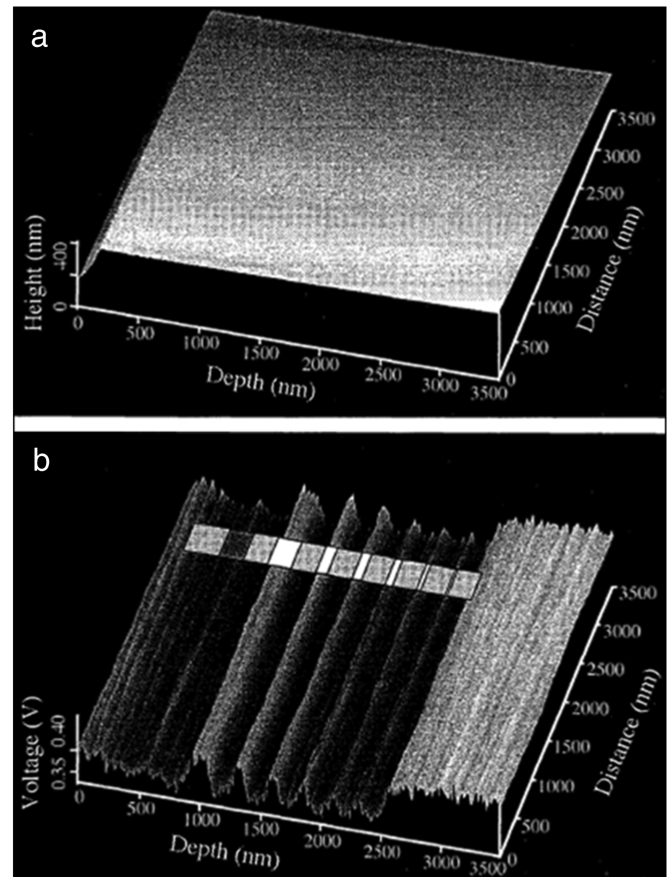

Fig. 30. KPFM on InAlAs/InGaAs multi-junction structure. (a) Topography and (b) CPD image of the cleaved InAlAs/InGaAs. InAlAs layers ranging from 20 to 200 nm thickness sandwiched between 200 nm layers of InGaAs. The spatial resolution of KPFM is determined with a cleaved multi-junction structure with varying layer thicknesses.
Source: Adapted from [95].

relatively little effect on the air-cleaved GaAs devices, making GaAs a suitable semiconductor material for two-dimensional potential profiles of air-cleaved operational devices. The potential profiles of a cross-sectional GaAs MESFET, for a drain-to-source voltage of 1, 2 and 3 V, and a gate bias of −1 V, are shown in Fig. 31. With increasing drain-to-source voltage, the potential drop occurs primarily between the gate and drain. Simulations of MESFETs indicate that the breakdown voltage is almost independent of gate-drain length, because most of the voltage drop should occur at the gate edge. Matsunami et al. demonstrated the majority of the voltage drop does not occur at the gate edge, but evenly over the gate-drain region, as shown in Fig. 32 [72]. For the KPFM to match the expected potential profile, a large step in the measured potential profile should occur at the edge of the gate. The step should easily be resolved because the spatial resolution of KPFM is better than 10 nm, smaller than the gate-to-drain length of approximately 2 μm. The two-dimensional potential profiles of devices can provide feedback to the design team, by providing data needed to understand the effects of devices structures.

Ludeke et al. observed a dipole across the 3 nm thick HfO_2 dielectric in a metal oxide semiconductor capacitor (MOSCAP) gate stack cleaved in UHV [97]. An ideal gate stack should have no charge in the oxide, and the potential profile through the oxide should remain relatively flat. For the Si/HfO_2/poly-Si gate stack, a dip in the potential occurs at the n-Si/HfO_2 interface, at a peak on the HfO_2/poly-Si interface, suggesting the presence of fixed charges in the oxide or at the interfaces. The orientation of the CPD indicated electrons near the n-Si/HfO_2 interface and positive

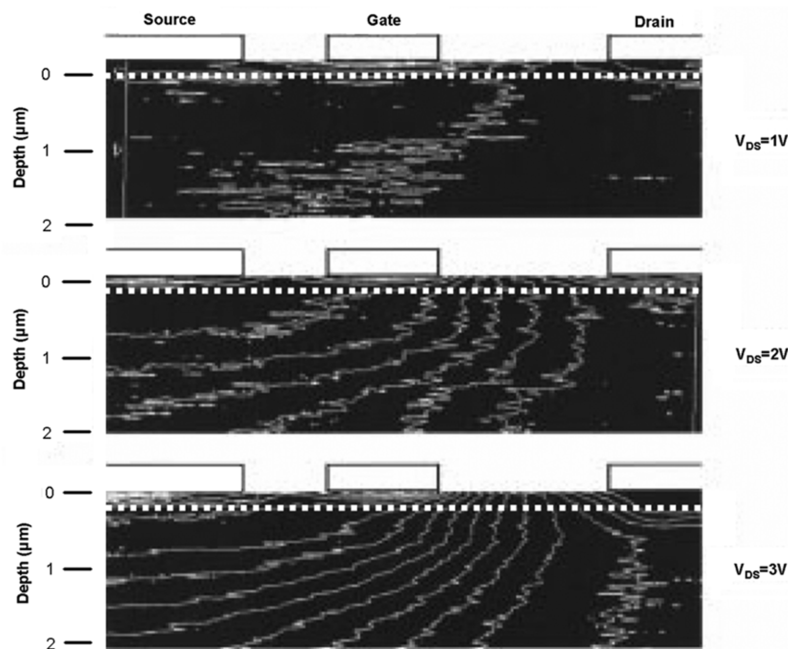

Fig. 31. Potential profiles of GaAs MESFETs with low temperature GaAs cap for 1, 2 and 3 V drain–source voltages (V_{DS}). The gate voltage is −1 V for all profiles. Contour lines are increments of 100 mV. White dashed lines indicate line profiles seen in Fig. 32. With increasing drain-to-source voltage, the potential drop appears to occur primarily between the gate and drain.
Source: Adapted from [72].

charges near the HfO_2/poly-interface, generating a static dipole across the dielectric.

KPFM helps describe the properties of thin oxide films to potentially explain the Fermi-energy level pinning at the interface. Ludeke et al. showed trapped positive and negative charges in SiO_2 and Al_2O_3 films grown on a Si substrate [98]. The trapped charge appears in the amorphous oxide film as dark spots for negative charges under negative substrate bias and positive charge for positive bias in potential images measured by KPFM. Al_2O_3 traps both positive and negative charges, while SiO_2 only traps negative charges.

KPFM is also used to study the electrical properties of surfaces/interfaces in devices to further understand trap states. KPFM provides insights into the simultaneous existence of positive and negative fixed charge in gate oxide films.

Another advantage of AFM based scanning probe systems is the diversity of materials compatible for investigation, from semiconductor materials to oxides to organics. KPFM has been performed on organic thin film transistors (OTFT) in UHV [70,71,99]. Bürgi et al. investigated the charge injection from the drain and source contacts into the active organic channel layer [70]. The contact resistances can be extracted from the localized voltage drop across the source–polymer (ΔV_s) or polymer–drain (ΔV_d) contacts. A large ΔV_s or ΔV_d indicates a poor contact, because less of the applied bias is used in the channel to drive the drain current.

Organic electronic devices are attractive due to low cost and great variety. However, low drive current is one of the limiting factors of organic materials in high performance applications, usually caused by poor contact resistances of 10 kΩ cm–10 MΩ cm [70]. KPFM can be used to optimize the contacts of the drain and source to the organic channels. Fig. 33 shows the potential profiles of poly(3-hexylthiophene) (P3HT) or F8T2 OTFTs, with various drain/source contact materials. The Cr–Au drain/source contacts show better charge injection for P3HT than Cr contacts. The voltage drop across the source/polymer for the Cr source is significantly larger, indicating poor contact. Another notable difference between the profiles of Cr–Au and Cr contacts is the symmetry of the potential drops at the contacts. For the good contacts,

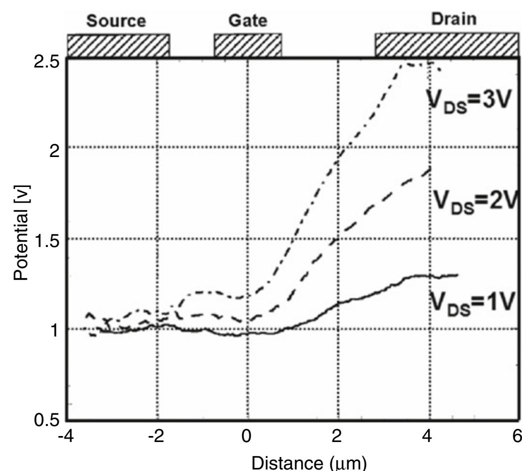

Fig. 32. Line profiles of dashed lines in Fig. 31 for various drain–source voltages (V_{DS}) of 1, 2 and 3 V. The gate voltage is −1 V for all profiles. The potential drop is expected to occur mainly at the gate edge because of an electric field build up. KPFM provides an intuitive picture of the device operation, assisting design teams in optimizing device performance.
Source: Adapted from [72].

Cr–Au, ΔV_s or ΔV_d are nearly identical, indicating that the contact resistance is dominated by the bulk mobility of the polymer. In the Cr case, the contact resistance is dominated by carrier injection, causing an asymmetric contact resistance. The asymmetric resistance is not caused by the source and drain contact resistance being different. If the contacts are reversed, the profile switches, as seen in inset of Fig. 33(b).

KPFM can provide an alternative to spreading resistance (SR) methods for measure doping profiles [81,88]. Tanimoto et al. performed KPFM on an air cleaved p^+n structures under illumination at the edge of the implantation mask to observe the doping profile for activated boron impurities [88]. The measurement was performed under illumination to reduce the surface band bending in the p^+ region. The photo-generated carriers drift to the surface,

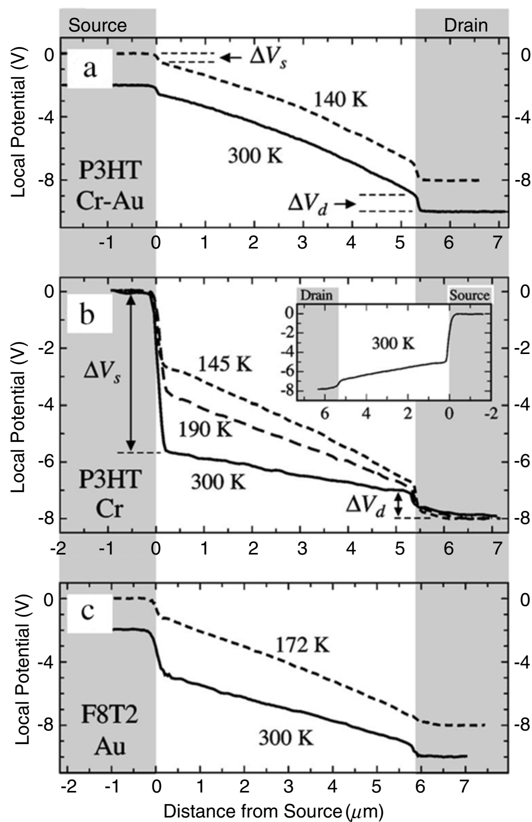

Fig. 33. CPD measurement on P3HT transistors. (a) Potential profiles of a P3HT transistor with Cr–Au source/drain contacts (gate voltage: 20 V and drain voltage: −8 V). (b) Potential profiles of a P3HT transistor with Cr source/drain contacts (gate voltage: −40 V and drain voltage: −8 V). (c) Potential profiles of a P8T2 transistor with Au source/drain contacts (gate voltage: −40 V and the drain voltage: −8 V). KPFM can be used to show the contact properties of different materials, which can be used to identify the optimal contact materials.
Source: Adapted from [70].

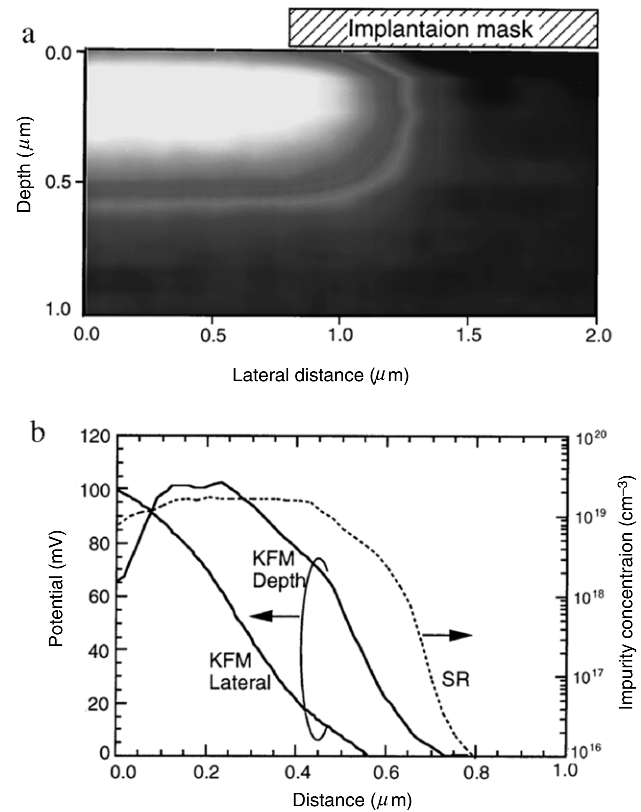

Fig. 34. KPFM of activate boron implantation. (a) Measured KPFM profile for a Si-$p^{+}n$ structure after active boron implantation. (b) Lateral and depth profiles for measured KPFM (solid line) and depth profile from measured SR (dotted line). KPFM provides an alternative method to measure dopant profiles.
Source: Adapted from [88].

depending on whether the material is n-type or p-type, as previously illustrated in Fig. 27(b) [82]. Fig. 34(a) shows the measured KPFM profile. A slight shift in the measured KPFM versus a SR measurement is seen in Fig. 34(b). The shift in profiles between KPFM and SR is attributed to surface band bending, even under illumination. The SR method gives a surface independent measurement of the dopant profile. KPFM, however, provides a two-dimensional profile, adding valuable processing information. Hochwitz et al. used KPFM to distinguished proper implanted bipolar junctions from failed implantations [100]. Defective devices show a clear decrease of 0.4 eV in the p-region potentials.

The yield of MOS devices can be studied with KPFM in planar imaging by measuring the probe capacitance over the channels of devices. Hochwitz et al. investigated CMOS memory chips with KPFM to identify failed devices [100]. The capacitance profiles extracted from the KPFM measurements showed devices with reduced probe-sample capacitances, indicating a failure in the channel dopants.

3.3.4. Solar cells

Development of photovoltaics focuses on efficiency and cost. One material showing a promising mix of low cost and high efficiency is chalcopyrites thin films. KPFM is a powerful tool for studying these systems, especially the band offsets and surface properties. Cu(In, Ga)(S, Se)$_2$ (CIGSSe) or CuGaSe$_2$ (CGSe) chalcopyrite solar cells have been studied with KPFM to determine band alignment [101–103] and grain boundary potential profiles [104–106].

Cross-sectional and surface KPFM on CIGSSe [103] or CGSe [101] is performed under illumination to observe the surface work function changes induced by the absorbed photons and to explore the surface properties, to help improve solar cell device performance. Employing KPFM, Sadewasser et al. studied the surface of a CIGSSe thin film on a ZnSe substrate in UHV [103]. The potential contrast is nearly unchanged under illumination. However, the average work function of the cleaved CIGSSe surface changes from 5.29 ± 0.12 eV (dark) to 4.83 ± 0.08 eV (when illuminated). Sadewasser et al. observes less surface band bending for air exposed cleaves over UHV cleaved samples. This indicates different cleaning methods can produce different surface electronic properties.

When analyzing the work function measured by KPFM, checking the amount of band bending with surface photovoltage (SPV) or ultraviolet photoelectron spectroscopy (UPS) is important in determining if the measured CPD values are highly affected by surface states. Glatzel et al. showed the work function of CGSe solar cells differ for untreated, annealed, and sputtered samples, consistent with different surface reconstructions and defect densities for the different surface treatments [101]. An increase in CPD contrast (from 570 to 900 mV) under dark conditions is observed after a 60 min Ar ion sputter cleaning. SPV or UPS measurements can complement KPFM by quantifying the band bending present from surface states, and by helping to determine the best preparation for the surface potential profile to match the bulk potentials.

Glatzel et al. performed a cross-sectional KPFM study on CIGSSe-based solar cells with a 100 nm $Zn_{1-x}Mg_xO$ or i-ZnO layer between the active CIGSSe layer and the ZnO:Ga window [102]. Fig. 35(a) illustrates the CPD overlaid on the topography of a cleaved CIGSSe solar cell. In the cross-sectional solar cell, each layer

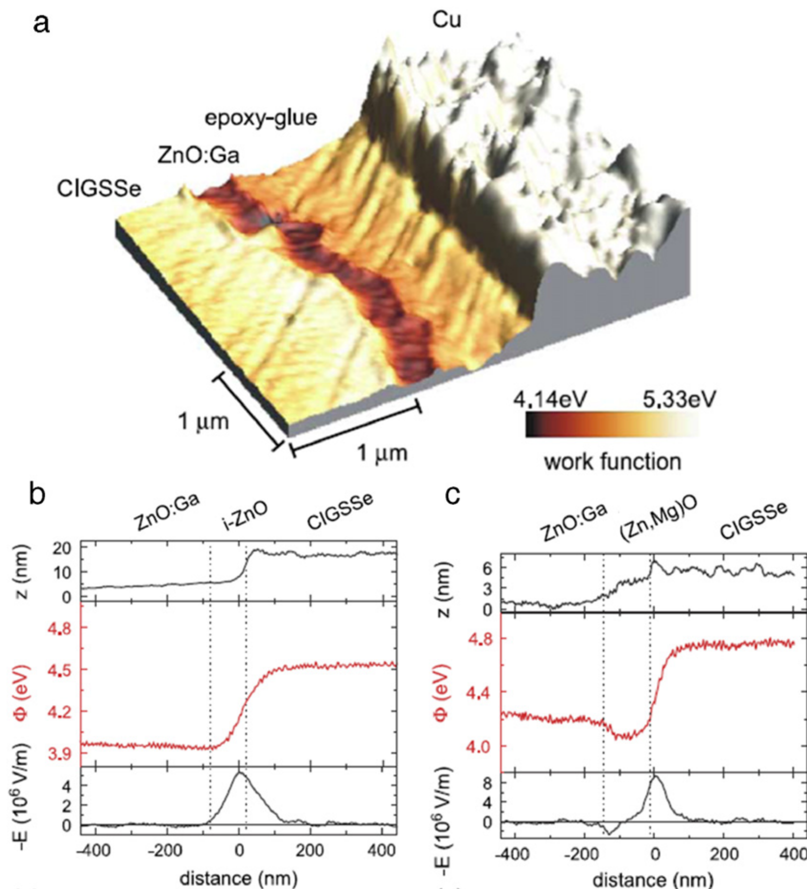

Fig. 35. Cross-sectional KPFM on CIGSSe solar cell. (a) 3D 3.2 × 2.5 μm CPD overlain on the topography of a cleaved CIGSSe solar cell with ZnO:Ga window layer. The light tan region is the CIGSSe followed by the ZnO:Ga in dark brown. The epoxy-glue is a medium tan color under the bright white Cu layer. (b) Topography, work function and electric field line profiles of the CIGSSe/i-ZnO/ZnO:Ga interface. (c) Topography, work function and electric field line profiles of the CIGSSe/$Zn_{1-x}Mg_xO$/ZnO:Ga interface. For the i-ZnO, only a potential changes is observed at the interface with CIGSSe where $Zn_{1-x}Mg_xO$ has potential changes at both interfaces. The depletion widths are increased in the i-ZnO case compared to the $Zn_{1-x}Mg_xO$ case. (For interpretation of the references to colour in this figure legend, the reader is referred to the web version of this article.)
Source: Adapted from [102].

can clearly be distinguished by the work function differences. Higher resolution cross-sectional KPFM performed on the CIGSSe/window interface indicated a difference in potential profile for different window materials, $Zn_{1-x}Mg_xO$ and i-ZnO. Fig. 35(b) and (c) show line profiles of the topography, work function and electric fields for i-ZnO and $Zn_{1-x}Mg_xO$, respectively. The $Zn_{1-x}Mg_xO$ layer shows a dip in the work function relative to the ZnO:Ga window layer. The other notable difference between $Zn_{1-x}Mg_xO$ and i-ZnO is the space charge regions for $Zn_{1-x}Mg_xO$ cells are smaller. The space charge layer is approximated by the stretch-out of the work function steps. The i-ZnO solar cell has depletion widths of $W_p = 130 \pm 40$ nm (W_p is depletion width in the p-type material) and $W_n = 100 \pm 30$ nm, (W_n is depletion width in the n-type material), while the $Zn_{1-x}Mg_xO$ cell has widths of $W_p = 100 \pm 40$ nm and $W_n = 70 \pm 40$ nm. The space charge region seems to extend more into the absorber layer for the $Zn_{1-x}Mg_xO$ cell, because of a slight shift in the peak of the electric field. The shift is within the resolution limits, but could explain the higher efficiency compared to the i-ZnO cells. With the high spatial resolution of 30 nm, KPFM can provide details about the depletion regions in the junctions for solar cells. Knowing the depletion widths and their positions helps to maximize design of the active regions in a solar cell.

For high efficiency solar cells, the texture or surface orientation strongly influences cell performance. Sadewasser et al. studied CGSe thin films on ZnSe(110) and CGSe on Mo/glass substrates [106]. KPFM was employed to show the work function of a thin film is correlated with the crystal growth plane as seen in Fig. 36. The work function difference between the crystal faces is caused by surface dipoles [32]. The crystal orientation of these films is critical to proper band alignment between the CGSe film and the contacts, to maximize efficiency. Fig. 36(a) and (b) show the topography and work function of the CGSe film on the ZnSe substrate. Fig. 36(c) shows the CPD overlaid on the topography, clearly showing each crystal face has the same work function as other crystal faces of identical symmetry. The crystal faces are identified by the angles of the planes in the topography relative to the (220) direction, and the (220) direction is known to be perpendicular to the surface, from X-ray diffraction studies. The work function of each crystalline plane is listed in Table 3.

Cu(In, Ga)Se_2 (CIGS) have shown higher efficiencies for films with (220/204)-texture. Hanna et al. used KPFM to show (220/204)-textured CIGS films do not exhibit work function spikes or dips at grain boundaries, as do random textured CIGS films. Random textured CIGS films show a 400 meV dip occurring at the grain boundary, while the grains have a work function of 5.44 eV. The (220/204)-textured CIGS films have small work function spikes at grain boundaries and exhibit several different work function levels. The grain boundaries for the random texture films have positive charges, which can attract electrons and promote recombination. The grain boundaries on (220/204)-textured CIGS films display negative charges which would repel electrons and might account for the increased efficiency. The space charge region of the grain boundaries is also dependent on sample type. A perfect

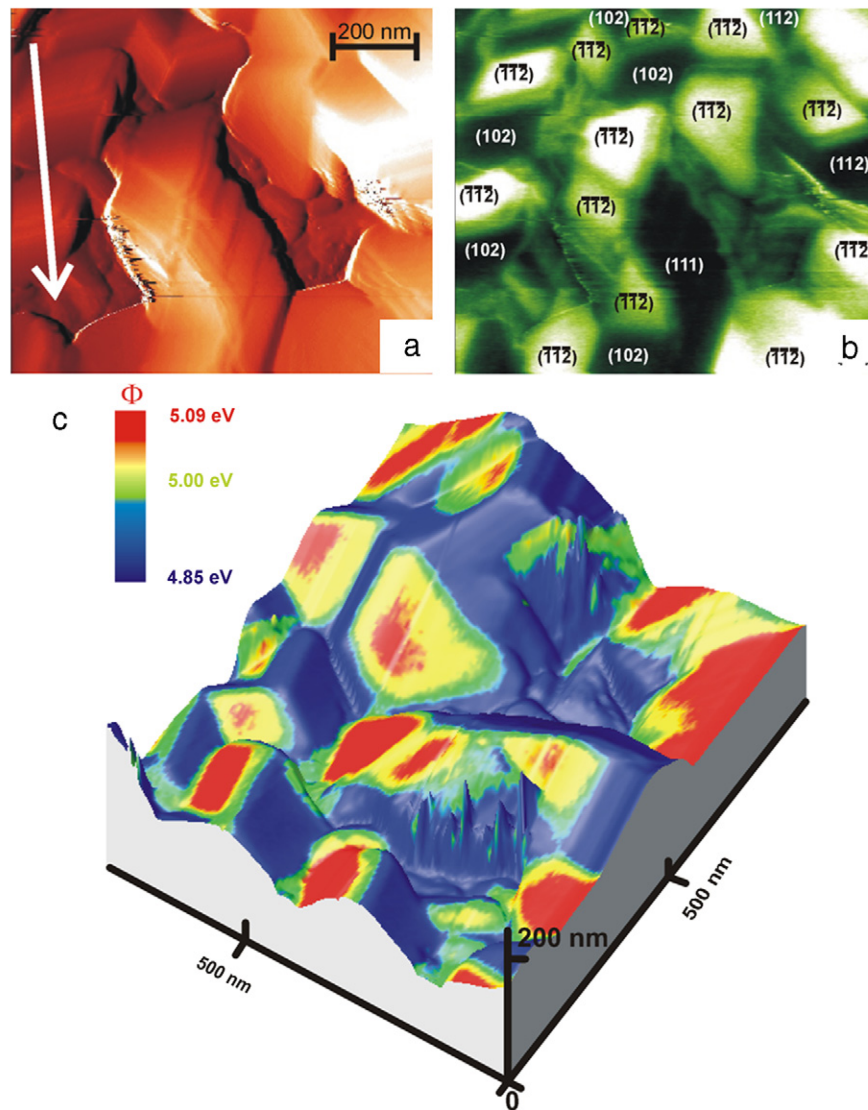

Fig. 36. KPFM on the surface of a CGSe solar cell. (a) Topography and (b) CPD of CGSe grown on cleaved ZnSe(110). The crystal faces are identified by the angles of the planes in the topography relative to the (220) direction, and the (220) direction is known to be perpendicular to the surface from X-ray diffraction studies. (c) Three-dimensional image overlaying the CPD values on the topographical image. Notice the sample crystal faces have the same CPD values, attributing a surface work function for each crystal face seen in Table 3. The work function of the tip is 4.28 ± 0.07 eV.
Source: Adapted from [106].

Table 3
Measured CPD values for different crystal facets of the thin film CGSe on either ZnSe or Mo/glass substrates. The work function of the tip is 4.28 ± 0.07 eV.
Source: Adapted from [106].

Sample	Surface orientation	CPD (mV)	Work function (eV)
$CuGaSe_2$/ZnSe	$(\bar{1}\bar{1}\bar{2})$	778 ± 22	5.06 ± 0.07
	(112)	590 ± 10	4.87 ± 0.07
	(102)	590 ± 10	4.87 ± 0.07
	(111)	560 ± 10	4.84 ± 0.07
$CuGaSe_2$/Mo/Glass	$(\bar{1}\bar{1}\bar{2})$	1195 ± 12	5.47 ± 0.07
	(112)	1019 ± 7	5.30 ± 0.07
	(110)	930 ± 5	5.21 ± 0.07

demonstration of the power of KPRM uses spatially resolved CPD to reveal specific information on the fixed charge buildup mechanism.

Sadewasser et al. observed a decrease in potential change at the grain boundaries and the space charge region, caused by the grain boundaries in CGSe and CIGS thin film solar cells [104]. The CGSe film shows a 110 ± 24 meV drop in the work function at the grain boundary with a space charge layer of 42 ± 10 nm in dark condition. Using the potential change at the grain boundary and the space charge width, the net doping of the absorber material and the trap state density at the grain boundary are estimated to be 9×10^{16} cm^{-3} and 8×10^{11} cm^{-2}. The CIGS films show a similar drop at the grain boundaries of 117±26 meV, but the average space charge is almost double at 82 ± 13 nm. These changes correspond to a doping decrease in the absorber material and a decrease in trap density to 3×10^{16} cm^{-3} and 4×10^{11} cm^{-2}, respectively.

Under illumination, the CGSe shows a decrease in the potential dip at the grain boundaries to 76 $\pm$ 30 meV and a slight increase in the space charge width of 56 $\pm$ 10 nm. The decrease in barrier height will assist charge transfer across a grain boundary, which is optimized for best efficiency.

KPFM has been used successfully to study CGSe and CIGS materials, and should see further use on other crystalline film solar cells to describe transport properties on the surface of the films. The potential dips and space charges widths measured by KPFM determine trap densities at grain boundaries with high accuracy. KPFM provides a non-invasive technique to measure the surface potential distribution in solar cell devices. The KPFM results help optimize the charge separation and its contribution to the production of photocurrents. KPFM also helps provide a picture of the potential profiles present in the stack structure and gives information about interface properties and band alignments. This information is used to optimize the efficiency of the cells. Other solar cell systems, besides chalcopyrites, have been investigated with KPFM, including organic solar cells [2] and complex III–V stacks [107]. The future development and implementation of low cost, high efficiency solar cells will be strongly dependent on techniques employed to study the systems in various ways. KPFM will play a large role in the understanding of new material systems for solar applications.

4. Concluding remarks

In past decade, KPFM has been developed to impact surface/material science and a variety of semiconductor industries. In this review, various aspects of KPFM including theory, instrumentation, and application have been provided. Throughout this article, the high spatial and energy resolution of KPFM for studying physical and chemical properties of surfaces, has been emphasized. Recent progress of atomic resolution KPFM in both theory (the concept of LCPD) and experimental results showing atomic potential distributions on ionic and semiconductor surfaces, has been explored. Details of KPFM instrumentation and operational principles comparing AM and FM mode, and comparision of KPFM to other surface potential measurement tools were presented. While the high-resolution was emphasized, several limitations of KPFM were also pointed out. Various applications of KPFM were showcased. Due to the increasing use of KPFM in multitudes of scientific and technological areas, not all applications could be included.

Simultaneous mapping of topography and potential (or work function) positions KPFM as a unique tool to characterize the electrical properties of metallic and semiconducting nanostructures. KPFM has successfully resolved an electron charging state on atomic scale. The range of applications of KPFM has been shown in the variety of samples and structures studied. including QDs, organic devices, multi-junction heterostructures, solar cells and devices under external biasing.

KPFM shows an interesting advantage in the study of smaller devices. Surface impact devices perform better at smaller scales, and KPFM is very sensitive to surface properties. KPFM becomes an ideal tool to probe nanostructures for electronic properties. In this respect, KPFM performed in UHV can provide an advantage over in-air KPFM because UHV avoids contaminates that may perturb the potential profiles. KPFM can provide critical information about surface potential distribution, which can help increase solar cell's efficiencies and device performance. Due to the versatility of KPFM to characterize electrical/electronic properties of surface and working devices, we believe KPFM will be used by a variety of scientific researchers in the future. However, the fundamental physics, specifically electrostatic interaction between tip and sample on the atomic scale, needs to be further elucidated, for broader application of atomic-resolution KPFM.

Acknowledgements

The authors would like to thank our colleagues, Joon-Sung Lee, James E. Royer, Erik D. Kappe and Tobin Kaufman-Osborn (Dept. of Chemistry and Material Science & Engineering Program, UCSD) for their numerous fruitful discussions to organize a large volume of KPFM application. The authors would also like the thank David Melitz for the manuscript proofreading. Sangyeob Lee gratefully acknowledges Dr. Ungdon Ham (Dept. of Physics, UCI) and Prof. Sehun Kim (Dept. of Chemistry, Korea Advanced Institute of Science and Technology) for various discussions about fundamental physics on scanning probe microscopy. Wilhelm Melitz would like to thank Prof. Prabhakar R. Bandaru (Dept. of Mechanical & Aerospace Eng., UCSD) and Prof. Charles W. Tu (Dept. Electrical & Computer Eng., UCSD) for their continued guidance and feedback, along with Prof. Edward T. Yu (Dept. Electrical & Computer Eng., U of Texas, Austin) for informative discussions. Jian Shen would like to thank Dr. Darby L. Feldwinn (Dept. of Chemistry, UCSB) and Dr. Yongmei Liu (Intel Corporation) for their mentorship, Dr. Matthias Passlack for his helpful discussions, and Dr. Niti Goel and Chomani K. Gaspe for providing testing samples.

References

[1] M. Nonnenmacher, M.P. Oboyle, H.K. Wickramasinghe, Appl. Phys. Lett. 58 (1991) 2921.
[2] H. Hoppe, T. Glatzel, M. Niggemann, A. Hinsch, M.C. Lux-Steiner, N.S. Sariciftci, Nano Lett. 5 (2005) 269.
[3] T. Hallam, C.M. Duffy, T. Minakata, M. Ando, H. Sirringhaus, Nanotechnology 20 (2009) 025203.
[4] L.M. Liu, G.Y. Li, Appl. Phys. Lett. 96 (2010) 083302.
[5] N.G. Clack, K. Salaita, J.T. Groves, Nat. Biotechnol. 26 (2008) 825.
[6] E. Finot, Y. Leonenko, B. Moores, L. Eng, M. Amrein, Z. Leonenko, Langmuir 26 (2010) 1929.
[7] R. Garcia, R. Perez, Surf. Sci. Rep. 47 (2002) 197.
[8] F.J. Giessibl, Rev. Modern Phys. 75 (2003) 949.
[9] T.R. Albrecht, P. Grutter, D. Horne, D. Rugar, J. Appl. Phys. 69 (1991) 668.
[10] C. Loppacher, M. Bammerlin, F. Battiston, M. Guggisberg, D. Muller, H.R. Hidber, R. Luthi, E. Meyer, H.J. Guntherodt, Appl. Phys. A 66 (1998) S215.
[11] R. Shikler, T. Meoded, N. Fried, B. Mishori, Y. Rosenwaks, J. Appl. Phys. 86 (1999) 107.
[12] S.V. Kalinin, A. Gruverman (Eds.), Scanning Probe Microscopy, Springer, New York, 2007.
[13] S. Hudlet, M. Saintjean, B. Roulet, J. Berger, C. Guthmann, J. Appl. Phys. 77 (1995) 3308.
[14] T. Glatzel, S. Sadewasser, M.C. Lux-Steiner, Appl. Surf. Sci. 210 (2003) 84.
[15] U. Zerweck, C. Loppacher, T. Otto, S. Grafstrom, L.M. Eng, Phys. Rev. B 71 (2005) 125424.
[16] G.H. Enevoldsen, T. Glatzel, M.C. Christensen, J.V. Lauritsen, F. Besenbacher, Phys. Rev. Lett. 100 (2008) 236104.
[17] L. Nony, F. Bocquet, C. Loppacher, T. Glatzel, Nanotechnology 20 (2009) 264014.
[18] C. Sommerhalter, T. Glatzel, T.W. Matthes, A. Jager-Waldau, M.C. Lux-Steiner, Appl. Surf. Sci. 157 (2000) 263.
[19] T. Arai, M. Tomitori, Phys. Rev. Lett. 93 (2004) 256101.
[20] K. Okamoto, K. Yoshimoto, Y. Sugawara, S. Morita, Appl. Surf. Sci. 210 (2003) 128.
[21] F. Bocquet, L. Nony, C. Loppacher, T. Glatzel, Phys. Rev. B 78 (2008) 035410.
[22] A. Sasahara, H. Uetsuka, H. Onishi, Japan J. Appl. Phys. 1 (43) (2004) 4647.
[23] F. Krok, K. Sajewicz, J. Konior, M. Goryl, P. Piatkowski, M. Szymonski, Phys. Rev. B 77 (2008) 235427.
[24] S. Kitamura, M. Iwatsuki, Appl. Phys. Lett. 72 (1998) 3154.
[25] S. Lee, A. Shinde, R. Ragan, Nanotechnology 20 (2009) 035701.
[26] S. Kitamura, K. Suzuki, M. Iwatsuki, C.B. Mooney, Appl. Surf. Sci. 157 (2000) 222.
[27] C. Barth, C.R. Henry, J. Phys. Chem. C 113 (2009) 247.
[28] H.J. Leamy, J. Appl. Phys. 53 (1982) R51.
[29] S. Gunther, B. Kaulich, L. Gregoratti, M. Kiskinova, Prog. Surf. Sci. 70 (2002) 187.
[30] J.C. Gonzalez, K.L. Bunker, P.E. Russell, Appl. Phys. Lett. 79 (2001) 1567.
[31] H. Luth, Solid Surfaces, Interfaces and Thin Films, 4th ed., Springer, Berlin, 2001.
[32] W. Monch, Semiconductor Surfaces and Interfaces, 2nd ed., Springer, Berlin, 1995.
[33] D.P. Woodruff, T.A. Delchar, Modern Techniques of Surface Science, Cambridge University Press, Cambridge, 1986.
[34] S. Sadewasser, C. Leendertz, F. Streicher, M.C. Lux-Steiner, Nanotechnology 20 (2009).
[35] K. Wandelt, Appl. Surf. Sci. 111 (1997) 1.

[36] L. Nony, A.S. Foster, F. Bocquet, C. Loppacher, Phys. Rev. Lett. 103 (2009) 036802.
[37] K. Okamoto, Y. Sugawara, S. Morita, Appl. Surf. Sci. 188 (2002) 381.
[38] T. Shiota, K. Nakayama, Japan J. Appl. Phys. 2 (41) (2002) L1178.
[39] A. Sasahara, C.L. Pang, H. Onishi, J. Phys. Chem. B 110 (2006) 17584.
[40] J.B. Clemens, S.R. Bishop, D.L. Feldwinn, R. Droopad, A.C. Kummel, Surf. Sci. 603 (2009) 2230.
[41] K. Okamoto, Y. Sugawara, S. Morita, Japan J. Appl. Phys. 1 (42) (2003) 7163.
[42] S. Sadewasser, P. Jelinek, C.K. Fang, O. Custance, Y. Yamada, Y. Sugimoto, M. Abe, S. Morita, Phys. Rev. Lett. 103 (2009) 266103.
[43] M. Valden, X. Lai, D.W. Goodman, Science 281 (1998) 1647.
[44] R.A. Bennett, P. Stone, M. Bowker, Cata. Lett. 59 (1999) 99.
[45] C.R. Henry, Appl. Surf. Sci. 164 (2000) 252.
[46] S.M. Nie, S.R. Emery, Science 275 (1997) 1102.
[47] M. Goryl, J.J. Kolodziej, F. Krok, P. Piatkowski, B. Such, M. Szymonski, Microelectron. Eng. 81 (2005) 394.
[48] G.W. Graham, Phys. Rev. B 32 (1985) 2640.
[49] C. Barth, C.R. Henry, Nanotechnology 17 (2006) S155.
[50] T. Glatzel, S. Sadewasser, R. Shikler, Y. Rosenwaks, M.C. Lux-Steiner, Mat. Sci. Eng. B 102 (2003) 138.
[51] C.R. Henry, Surf. Sci. Rep. 31 (1998) 235.
[52] B.K. Min, W.T. Wallace, A.K. Santra, D.W. Goodman, J. Phys. Chem. B 108 (2004) 16339.
[53] C. Barth, C.R. Henry, Appl. Phys. Lett. 89 (2006) 252119.
[54] B. Yoon, H. Hakkinen, U. Landman, A.S. Worz, J.M. Antonietti, S. Abbet, K. Judai, U. Heiz, Science 307 (2005) 403.
[55] H.G. Boyen, et al., Science 297 (2002) 1533.
[56] U. Heiz, W.D. Schneider, J. Phys. D 33 (2000) R85.
[57] M. Haruta, Catal. Today 36 (1997) 153.
[58] L. Gross, F. Mohn, P. Liljeroth, J. Repp, F.J. Giessibl, G. Meyer, Science 324 (2009) 1428.
[59] J. Repp, G. Meyer, F.E. Olsson, M. Persson, Science 305 (2004) 493.
[60] F.J. Giessibl, Appl. Phys. Lett. 76 (2000) 1470.
[61] M.R. Hoffmann, S.T. Martin, W.Y. Choi, D.W. Bahnemann, Chem. Rev. 95 (1995) 69.
[62] A.L. Linsebigler, G.Q. Lu, J.T. Yates, Chem. Rev. 95 (1995) 735.
[63] A. Sasahara, K. Hiehata, H. Onishi, Catal. Surv. Asia 13 (2009) 9.
[64] K. Hiehata, A. Sasahara, H. Onishi, Nanotechnology 18 (2007) 084007.
[65] T. Glatzel, L. Zimmerli, S. Koch, S. Kawai, E. Meyer, Appl. Phys. Lett. 94 (2009) 063303.
[66] E. Meyer, T. Glatzel, Science 324 (2009) 1397.
[67] K. Nakayama, T. Shiota, Surf. Interface Anal. 40 (2008) 885.
[68] Y. Sugawara, T. Uchihashi, M. Abe, S. Morita, Appl. Surf. Sci. 140 (1999) 371.
[69] A. Huijser, J. Vanlaar, T.L. Vanrooy, Surf. Sci. 62 (1977) 472.
[70] L. Burgi, T.J. Richards, R.H. Friend, H. Sirringhaus, J. Appl. Phys. 94 (2003) 6129.
[71] L. Burgi, H. Sirringhaus, R.H. Friend, Appl. Phys. Lett. 80 (2002) 2913.
[72] K. Matsunami, T. Takeyama, T. Usunami, S. Kishimoto, K. Maezawa, T. Mizutani, M. Tomizawa, P. Schmid, K.M. Lipka, E. Kohn, Solid-State Electron. 43 (1999) 1547.
[73] T. Mizutani, M. Arakawa, S. Kishimoto, Iedm — International Electron Devices Meeting, Technical Digest 1996 (1996) 31.
[74] T. Mizutani, M. Arakawa, S. Kishimoto, IEEE Electron Device Lett. 18 (1997) 423.
[75] M.A. Salem, H. Mizuta, S. Oda, Appl. Phys. Lett. 85 (2004) 3262.
[76] T. Yamauchi, M. Tabuchi, A. Nakamura, Appl. Phys. Lett. 84 (2004) 3834.
[77] S. Shusterman, A. Raizman, A. Sher, Y. Paltiel, A. Schwarzman, E. Lepkifker, Y. Rosenwaks, Nano Lett. 7 (2007) 2089.
[78] Y. Martin, D.W. Abraham, H.K. Wickramasinghe, Appl. Phys. Lett. 52 (1988) 1103.
[79] J.M.R. Weaver, D.W. Abraham, J. Vac. Sci. Technol. B 9 (1991) 1559.
[80] J.M.R. Weaver, H.K. Wickramasinghe, J. Vac. Sci. Technol. B 9 (1991) 1562.
[81] A.K. Henning, T. Hochwitz, J. Slinkman, J. Never, S. Hoffmann, P. Kaszuba, C. Daghlian, J. Appl. Phys. 77 (1995) 1888.
[82] T. Mizutani, T. Usunami, S. Kishimoto, K. Maezawa, Japan J. Appl. Phys. 1 (38) (1999) 4893.
[83] S. Saraf, Y. Rosenwaks, Surf. Sci. 574 (2005) L35.
[84] R. Shikler, T. Meoded, N. Fried, Y. Rosenwaks, Appl. Phys. Lett. 74 (1999) 2972.
[85] A. Kikukawa, S. Hosaka, R. Imura, Appl. Phys. Lett. 66 (1995) 3510.
[86] C. Loppacher, U. Zerweck, S. Teich, E. Beyreuther, T. Otto, S. Grafstrom, L.M. Eng, Nanotechnology 16 (2005) S1.
[87] T. Meoded, R. Shikler, N. Fried, Y. Rosenwaks, Appl. Phys. Lett. 75 (1999) 2435.
[88] M. Tanimoto, O. Vatel, J. Vac. Sci. Technol. B 14 (1996) 1547.
[89] F. Robin, H. Jacobs, O. Homan, A. Stemmer, W. Bachtold, Appl. Phys. Lett. 76 (2000) 2907.
[90] A.V. Ankudinov, V.P. Evtikhiev, E.Y. Kotelnikov, A.N. Titkov, R. Laiho, J. Appl. Phys. 93 (2003) 432.
[91] A. Chavezpirson, O. Vatel, M. Tanimoto, H. Ando, H. Iwamura, H. Kanbe, Appl. Phys. Lett. 67 (1995) 3069.
[92] T. Mizutani, T. Usunami, S. Kishimoto, K. Maezawa, Japan J. Appl. Phys. 2 (38) (1999) L767.
[93] A. Schwarzman, E. Grunbaum, E. Strassburg, E. Lepkifker, A. Boag, Y. Rosenwaks, T. Glatzel, Z. Barkay, M. Mazzer, K. Barnham, J. Appl. Phys. 98 (2005) 084310.
[94] G. Leveque, P. Girard, E. Skouri, D. Yarekha, Appl. Surf. Sci. 157 (2000) 251.
[95] T. Usunami, M. Arakawa, S. Kishimoto, T. Mizutani, T. Kagawa, H. Iwamura, Japan J. Appl. Phys. 1 (37) (1998) 1522.
[96] M. Arakawa, S. Kishimoto, T. Mizutani, Japan J. Appl. Phys. 1 (36) (1997) 1826.
[97] R. Ludeke, V. Narayanan, E.P. Gusev, E. Cartier, S.J. Chey, Appl. Phys. Lett. 86 (2005) 122901.
[98] R. Ludeke, J. Non-Cryst. Solids 303 (2002) 150.
[99] J.A. Nichols, D.J. Gundlach, T.N. Jackson, Appl. Phys. Lett. 83 (2003) 2366.
[100] T. Hochwitz, et al., J. Vac. Sci. Technol. B 14 (1996) 440.
[101] T. Glatzel, D.F. Marron, T. Schedel-Niedrig, S. Sadewasser, M.C. Lux-Steiner, Appl. Phys. Lett. 81 (2002) 2017.
[102] T. Glatzel, H. Steigert, S. Sadewasser, R. Klenk, M.C. Lux-Steiner, Thin Solid Films 480 (2005) 177.
[103] S. Sadewasser, T. Glatzel, M. Rusu, A. Meeder, D. Fuertes Marron, A. Jager-Waldau, M.C. Lux-Steiner, Mat. Res. Soc. Symp. P. 668 (2001) H5.4.1.
[104] S. Sadewasser, T. Glatzel, S. Schuler, S. Nishiwaki, R. Kaigawa, M.C. Lux-Steiner, Thin Solid Films 431 (2003) 257.
[105] G. Hanna, T. Glatzel, S. Sadewasser, N. Ott, H.P. Strunk, U. Rau, J.H. Werner, Appl. Phys. A 82 (2006) 1.
[106] S. Sadewasser, T. Glatzel, M. Rusu, A. Jager-Waldau, M.C. Lux-Steiner, Appl. Phys. Lett. 80 (2002) 2979.
[107] C.S. Jiang, H.R. Moutinho, D.J. Friedman, J.F. Geisz, M.M. Al-Jassim, J. Appl. Phys. 93 (2003) 10035.